Petroleum Science 23 (2026) 2046–2065

Contents lists available at ScienceDirect

Petroleum Science

journal homepage: www.keaipublishing.com/en/journals/petroleum-science

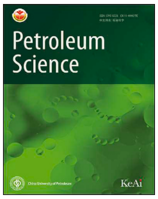

Original Paper

Biomass-derived amphiphilic nitrogen-doped carbon dots: Molecular design, interfacial regulation, and enhanced oil recovery performance

Yu Wu [a,b], Yan-Cheng Zheng [a,b,*], Jian Mu [a,b], Fu-Chang You [a,b,**], Zheng-Yu Li [a,b]

[a] *College of Chemistry & Environmental Engineering, Yangtze University, Jingzhou, 434023, Hubei, China*
[b] *Hubei Engineering Research Centers for Clean Production and Pollution Control of Oil and Gas Fields, Jingzhou, 434023, Hubei, China*

ARTICLE INFO

Article history:
Received 7 July 2025
Received in revised form
5 December 2025
Accepted 5 December 2025
Available online 11 December 2025

Edited by Yan-Hua Sun

Keywords:
Nanofluid flooding
Amphiphilic carbon dots
Surface functionalization
Interfacial regulation
Enhanced oil recovery
Low-permeability reservoirs

ABSTRACT

In response to the overlooked influence of precursor molecular structure on interfacial performance in the application of amphiphilic carbon dots (CDs) for enhanced oil recovery (EOR), this study synthesized nitrogen-doped CDs (NCDs, FG, and TA series) using biomass-derived precursors via carbonization, amidation, quaternization, and alkylation. The relationships between precursor structure, surface functionality, interfacial behavior, and oil displacement performance were systematically investigated. TA-derived NCDs exhibited higher surface polarity and amphiphilicity due to abundant carboxyl groups, while increasing alkyl chain length enhanced hydrophobicity and suppressed surface defects. TA-NCDs-L16 showed the best interfacial properties, with a critical micelle concentration (CMC) of 0.104 g/L, γ_{CMC} of 24.71 mN/m, and zeta potential of +67.80 mV. Under NaCl concentrations ranging from 0 to 12 wt%, the oil–water interfacial tension decreased to a minimum of 0.00151 mN/m, and the contact angle dropped to 16.3°, indicating excellent salt tolerance and wettability reversal capability. In low-permeability core flooding tests, TA-NCDs-L16 achieved a significantly enhanced final oil recovery of 60.42%, with a 27.26% increase in recovery and a 38.71% reduction in injection pressure. The improved EOR performance was attributed to ultra-low interfacial tension, the formation of high-density polar adsorption layers, and nanoscale size effects that enabled efficient pore-throat penetration and fluid redistribution, thereby facilitating the detachment and mobilization of residual oil. In high-salinity formation water containing Ca^{2+}/Mg^{2+} and under elevated temperatures (50–90 °C), further evaluation confirmed that the amphiphilic NCDs maintained strong interfacial activity and sustained wettability reversal. TA-NCDs-L16 retained an ultra-low interfacial tension (~0.002 mN/m) and stable wettability regulation even after 240 h of thermal aging at 80 °C, while core flooding still exhibited significant reductions in injection pressure and enhancements in oil recovery. This study clarifies the correlation among precursor structure, functional group configuration, interfacial behavior, and oil displacement efficiency, providing theoretical guidance and material design concepts for the development of carbon-based amphiphilic nanofluids in low-permeability reservoir applications.

1. Introduction

With the ongoing transformation of the global energy structure and the continuous advancement of unconventional oil and gas development, low-permeability tight reservoirs have become an increasingly important target in oilfield production (Meng et al., 2024; Sun et al., 2023). These reservoirs typically feature extremely small pore sizes, narrow throats, high capillary pressure, low permeability, and complex pore networks. As a result, strong wetting-induced adhesion occurs between crude oil and rock surfaces, leaving residual oil in the form of thin films or isolated droplets within the pores. This severely limits the effectiveness of conventional water flooding and poses a major challenge to improving the overall oil recovery factor (Hu et al., 2018; Liu et al., 2025). To overcome this limitation, the

---

* Corresponding author.
** Corresponding author.
E-mail addresses: zhengycg@yangtzeu.edu.cn (Y.-C. Zheng), yfc81@yangtzeu.edu.cn (F.-C. You).
Peer review under the responsibility of China University of Petroleum (Beijing).

https://doi.org/10.1016/j.petsci.2025.12.011

development of efficient interfacial regulation systems aimed at mobilizing residual oil has emerged as a key research direction in enhanced oil recovery (EOR) technologies for tight reservoirs (Joshi et al., 2025; Wu et al., 2021). However, polymer flooding systems, although widely applied, often encounter significant difficulties in low-permeability formations due to high injection pressure requirements, severe shear degradation within pore channels, and increased risks of pore blockage (AfzaliTabar et al., 2020; Zhao et al., 2024). Meanwhile, conventional surfactant systems tend to undergo hydrolysis, thermal decomposition, or excessive adsorption under high-temperature and high-salinity reservoir conditions. These shortcomings result in poor interfacial activity retention and limited sweep efficiency, thereby reducing their effectiveness in displacing residual oil trapped in nanopores and tight throats (Feng et al., 2022; Nourafkan et al., 2019). Therefore, it is of great significance to develop nanofluid systems with small particle sizes, good dispersibility, long-term interfacial regulation capability, and strong formation compatibility. Such systems are expected to offer more promising solutions for enhancing oil recovery from low-permeability reservoirs.

In recent years, the introduction of nanotechnology has opened new avenues for interfacial regulation in oil displacement. By utilizing nanoparticles to reduce oil–water interfacial tension, alter rock wettability, and promote film stripping, it is possible to effectively mobilize residual oil adhered to pore surfaces, enhance microscale fluid transport, and ultimately improve oil recovery efficiency (Li et al., 2018a; Lu et al., 2025; Zhou et al., 2020). Among the various nanomaterials explored for EOR, inorganic nanoparticles such as silicon dioxide (Yekeen et al., 2023), aluminum oxide (Keykhosravi and Simjoo, 2020), titanium dioxide (Zargar et al., 2020), copper oxide (Abbood et al., 2022), zirconium dioxide (Rezvani et al., 2018), magnesium oxide (Dibaji et al., 2022), and iron oxide (Toma et al., 2022) have attracted considerable attention. However, these inorganic nanoparticles typically possess particle sizes in the tens of nanometers range, making it difficult for them to access the nanopores within tight and structurally complex reservoirs (Lashari et al., 2022; Ngouangna et al., 2022; Wyss et al., 2006). Moreover, they tend to aggregate easily, exhibit poor dispersion stability, and pose a risk of pore plugging during injection. In addition, most of these nanoparticles lack inherent surface activity and require combination with surfactants to achieve desirable interfacial regulation performance (Li et al., 2023b; Zhao et al., 2018).

In comparison, carbon-based nanomaterials, especially carbon dots (CDs), have shown significant promise as the core components of emerging nanofluid systems for EOR (Fan et al., 2025; Zhou et al., 2025). Compared with traditional nanoparticles, CDs exhibit several unique advantages, including ultra-small particle size (less than 10 nm), abundant surface functional groups, excellent dispersibility, and tunable surface chemistry. These features allow CDs to be easily modified to achieve strong interfacial activity (Medina et al., 2024; Zhao et al., 2020). In oil displacement applications, amphiphilic CDs can rapidly migrate to the oil–water interface and effectively reduce interfacial tension. Through the modulation of surface polarity and hydrophobicity, they promote wettability alteration and reduce the adhesion strength of oil films on rock surfaces, thereby enhancing the detachment of residual oil trapped in micropores and narrow throats (Cai et al., 2025; Gao et al., 2025; Razavifar et al., 2024). In addition, the flexibility of surface modification provides CDs with good interfacial stability and sustained performance under high-temperature and high-salinity reservoir conditions (Lu et al., 2024; Shen et al., 2024). Recent studies have demonstrated that appropriate precursor selection and surface functionalization can significantly enhance the oil recovery performance of CDs in low-permeability reservoirs. For example, Wu et al. (2020) synthesized CDs from petroleum coke and modified them with the nonionic surfactant Tween 80, resulting in a 26.14% reduction in injection pressure in core flooding tests. In further work, the same group prepared CDs using a composite precursor of petroleum coke and asphalt, followed by electrochemical exfoliation and benzenesulfonate modification, which achieved a 27.88% increase in oil recovery under conditions of 100 °C and 140 g/L salinity (Wu et al., 2023). Liu et al. (2024) synthesized CDs from urea and citric acid, and modified them with oleyl amidopropyl betaine, achieving a recovery improvement of 31.1%. Cao et al. (2023a) produced CDs via a one-step hydrothermal method using glucose and 3-aminopropyltriethoxysilane, leading to a 21% increase in oil recovery, which outperformed both conventional silica nanoparticles and traditional surfactants. Despite these advances, most current studies focus on CDs derived from single types of precursors. There is still a lack of systematic understanding regarding how differences in precursor molecular structure influence the density and accessibility of functional sites on the carbon dot surface. In particular, the effects of precursor structure on the efficiency of introducing polar and non-polar functional groups, and their corresponding impacts on interfacial properties and oil displacement performance, remain unclear.

Based on the above, this study proposes a strategy that takes the molecular structure differences of precursors as a key variable to construct amphiphilic carbon dots with synergistically regulated surface functionalities. Fenugreek gum, a natural biomass rich in hydroxyl groups, and tartaric acid, a small molecule containing two carboxyl groups, were selected as representative precursors. Through a solvothermal carbonization process combined with amide-based nitrogen doping, the carbon dot core framework was constructed. Subsequently, surface modification was carried out through quaternization and long-chain alkyl group introduction, enabling the coordinated regulation of polar cationic site density and non-polar hydrophobic chain flexibility. The resulting amphiphilic carbon dots were systematically characterized and evaluated in terms of structural morphology, surface functional group composition, optical properties, interfacial activity, pH responsiveness, salt tolerance, and oil displacement performance in low-permeability core flooding tests. Particular emphasis was placed on elucidating the critical role of precursor molecular structure in determining the density and composition of surface functional groups. Furthermore, the structure–property relationships between carbon dot surface chemistry, interfacial activity, and microscale oil displacement behavior were clarified. This work provides new insights into the molecular design of amphiphilic carbon-based nanofluids and their application in interfacial regulation for enhanced oil recovery in tight reservoirs.

2. Experimental section

2.1. Materials

Fenugreek gum (99%) was purchased from Jiangsu Duo Young Biotechnology Co., Ltd. Tartaric acid (99.5%) was obtained from Anhui Apple Biological Technology Co., Ltd. Absolute ethanol (99.7%), ethyl acetate (99%), 3-dimethylaminopropylamine (99%), epichlorohydrin (99%), dodecylamine (98%), hexadecylamine (98%), sodium chloride (99.5%), and sodium hydroxide (98%) were all purchased from Shanghai Macklin Biochemical Technology Co., Ltd. Polydimethylsiloxane (average molecular weight 115,000 Da) was supplied by Shanghai Aladdin Biochemical Technology Co., Ltd. All chemicals were used as received without further purification. White oil was obtained from Sinopec Jingmen Petrochemical Company, with a saturated hydrocarbon content of 100%. DY crude oil and formation water were collected from the

Changqing Oilfield. The crude oil was composed of 62.51% saturates, 24.65% aromatics, 12.02% resins, and 0.82% asphaltenes. The formation water had a total salinity of 99,951.4 mg/L, with ionic composition of 15,457.7 mg/L Na^+/K^+, 21,564.2 mg/L Ca^{2+}, 202.3 mg/L Mg^{2+}, 62,278.5 mg/L Cl^-, 259.0 mg/L SO_4^{2-}, and 189.7 mg/L HCO_3^-, with a pH of approximately 6.3. Ultrapure water with a resistivity of 18.15 MΩ·cm was produced using a laboratory-grade water purification system.

2.2. Synthesis

A total of 1.0 g of fenugreek gum was added to a reactor containing 50 mL of absolute ethanol and dispersed by ultrasonication for 15 min. Then, 1.0 g of 3-dimethylaminopropylamine was slowly added dropwise under stirring. The mixture was further sonicated for 15 min. After sealing the reactor, the reaction was conducted at 180 °C for 12 h under an air atmosphere. Upon completion, the reaction mixture was cooled to room temperature and centrifuged at 10,000 rpm for 10 min to remove large particulate impurities. The supernatant was filtered through filter paper, and ethanol was removed by rotary evaporation at 60 °C. The concentrated product was redissolved in ultrapure water and filtered using a 0.22 μm membrane to eliminate residual large particles. The filtrate was transferred into a dialysis bag with a molecular weight cutoff of 1000 Da and dialyzed against ultrapure water at room temperature for 24 h, with the dialysis water replaced every 6 h. After dialysis, the retained solution was collected and vacuum-dried to obtain FG-NCDs.

For linker preparation, 1.0 g of dodecylamine was added to a round-bottom flask, followed by 20 mL of absolute ethanol. The mixture was sonicated for 15 min to ensure uniform dispersion. Under continuous stirring, 1.05 g of epichlorohydrin was added dropwise using a constant-pressure dropping funnel. The reaction was carried out at 25 °C for 10 h. After completion, unreacted reagents and ethanol were removed by rotary evaporation under reduced pressure. The resulting colorless viscous liquid was denoted as linker L12. Replacing dodecylamine with an equimolar amount of hexadecylamine under the same procedure yielded linker L16.

To functionalize the carbon dots, the as-prepared FG-NCDs were dissolved in 50 mL of absolute ethanol and sonicated for 15 min before being transferred to a round-bottom flask. Linker L12 was then added, and the mixture was stirred for 60 min, followed by heating at 80 °C for 12 h. After the reaction, ethanol was removed by rotary evaporation, and the residue was redissolved in ultrapure water. The resulting aqueous solution was transferred to a separatory funnel and extracted three times with ethyl acetate to remove unreacted components. The aqueous phase was collected and vacuum-dried to obtain the final product, designated FG-NCDs-L12. Replacing linker L12 with L16 under identical conditions yielded FG-NCDs-L16.

By replacing fenugreek gum with tartaric acid as the precursor and following the same synthetic procedures, the corresponding products TA-NCDs, TA-NCDs-L12, and TA-NCDs-L16 were obtained. A schematic illustration of the synthesis process is shown in Fig. 1.

2.3. Structural characterization

To comprehensively analyze the structural features, morphology, and optical properties of the biomass-derived amphiphilic NCDs, a combination of analytical techniques was employed. These included transmission electron microscopy (TEM), Fourier transform infrared spectroscopy (FT-IR), X-ray photoelectron spectroscopy (XPS), ultraviolet–visible absorption spectroscopy (UV–Vis), and photoluminescence (PL) spectroscopy. The morphology of the samples was examined using a JEOL JEM-F200 transmission electron microscope. Prior to measurement, 0.1 g/L aqueous solutions of carbon dots were ultrasonicated for 10 min. Then, 2–3 drops of the suspension were deposited onto copper grids coated with ultrathin carbon films. After natural drying, TEM images were captured at an accelerating voltage of 200 kV. FT-IR spectra were recorded using a Thermo Scientific IR-408 spectrometer. The dried samples were mixed with potassium bromide at an appropriate ratio, pressed into pellets under 10 MPa for 10 s, and scanned over a wavenumber range of 4000 to 500 cm^{-1} to identify surface functional groups. XPS measurements were carried out using a Thermo Scientific ESCALAB 250Xi spectrometer equipped with a monochromatic Al Kα source ($h\nu = 1486.6$ eV). The operating conditions were set at 12.5 kV and 16 mA. The pass energy was 20 eV for high-resolution spectra, with an energy step size of 0.05 eV. The C 1*s* peak at 284.8 eV was used as the reference for energy calibration. UV–Vis absorption spectra were obtained using a TU-1900 spectrophotometer (Persee General Instrument Co., Ltd., Beijing, China). The measurements were performed in the range of 190–600 nm using 0.1 g/L aqueous solutions, with ultrapure water as the reference. Photoluminescence properties were characterized using a Hitachi F-4700 fluorescence spectrophotometer.

2.4. Performance evaluation

2.4.1. Surface tension, hydrodynamic diameter, and zeta potential measurements

A series of aqueous solutions of FG-NCDs-L12, FG-NCDs-L16, TA-NCDs-L12, and TA-NCDs-L16 were prepared at an initial concentration of 1 g/L using ultrapure water and subsequently diluted to concentrations of 0.5, 0.25, 0.1, 0.05, 0.025, and 0.01 g/L. The surface tension of each solution was measured using a QBZY automatic surface tensiometer (Shanghai Fangrui Instrument Co., Ltd.). A γ–C curve was constructed by plotting surface tension (γ) versus concentration (C), and the critical micelle concentration (CMC) was determined from the intersection point of the two linear regions of the fitted curve. The hydrodynamic diameters of the four types of biomass-derived amphiphilic NCDs at concentrations of 0.01, 0.05, 0.1, 0.5, and 1 g/L were measured using a Zetasizer Nano ZS instrument (Malvern Panalytical Ltd., UK). To evaluate pH-responsive behavior, 0.5 g/L solutions of each NCD type were prepared and tested at pH values of 1, 3, 5, 7, 9, 11, and 13. Surface tension and zeta potential under these conditions were measured using the same tensiometer and Zetasizer, respectively. All measurements were conducted at 25 °C. Each test was performed in triplicate under identical conditions, and the average values were recorded.

2.4.2. Contact angle measurement

Glass slides were sequentially cleaned with ultrapure water and absolute ethanol 2 to 3 times, then dried in an oven at 60 °C for 3 h. After cooling to room temperature, the slides were immersed in a 10% sodium hydroxide solution for 4 h, followed by the same cleaning and drying procedures. The dried slides were then immersed in polydimethylsiloxane and maintained at 60 °C for 120 h to achieve oleophilic surface modification. After oleophilic treatment, the slides were immersed in solutions of FG-NCDs-L12, FG-NCDs-L16, TA-NCDs-L12, and TA-NCDs-L16 at concentrations of 0.01, 0.05, 0.1, 0.5, and 1 g/L, respectively. The immersion was conducted at a constant temperature of 60 °C for 24 h. The slides were then removed and air-dried at room temperature. Contact angle measurements were carried out at 25 °C using a JC2000C contact angle goniometer (Shanghai Zhongchen Digital

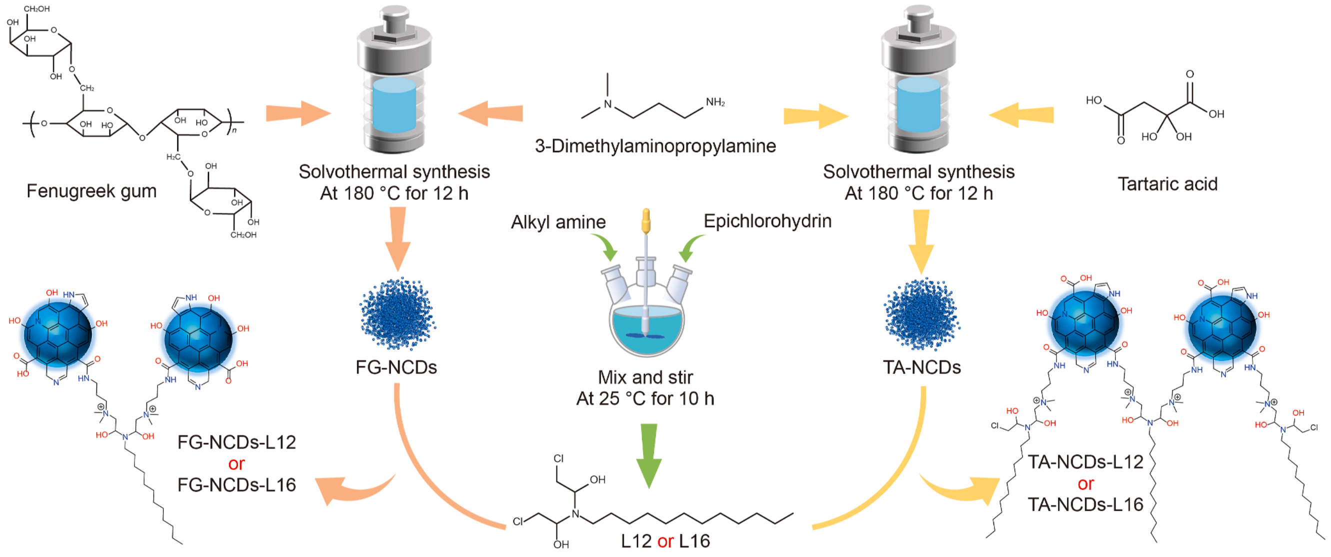

Fig. 1. Schematic illustration of the synthesis route for biomass-derived amphiphilic NCDs.

Technology Equipment Co., Ltd., China). The variation in contact angle of ultrapure water on the surface of each treated slide was recorded as a function of contact time. In addition, to better simulate reservoir conditions, solutions of FG-NCDs-L16 and TA-NCDs-L16 (0.5 g/L) were prepared using formation water. The oleophilic glass slides were immersed under two sets of conditions: (i) a fixed immersion time of 24 h with varying temperatures (50, 60, 70, 80, and 90 °C), and (ii) a fixed temperature of 80 °C with varying immersion durations (0, 24, 72, 120, 168, and 240 h). Contact angle measurements were subsequently performed following the same procedures described above. All measurements were repeated three times under identical conditions, and the average values were reported.

2.4.3. Oil–water interfacial tension measurement

The interfacial tension between oil droplets and aqueous NCD solutions was measured using the spinning drop method with a TX-500C interfacial tensiometer (CNG Enterprises Ltd., USA). White oil and DY crude oil were used as the oil phases, and FG-NCDs-L12, FG-NCDs-L16, TA-NCDs-L12, and TA-NCDs-L16 aqueous solutions with concentrations of 0.01, 0.025, 0.05, 0.1, 0.25, 0.5, and 1 g/L were used as the test fluids. Measurements were conducted at 60 °C with a rotation speed of 5000 rpm. In addition, to evaluate salt tolerance, interfacial tension was measured between white oil or DY crude oil droplets and 0.5 g/L aqueous solutions of each amphiphilic NCD sample containing various concentrations of sodium chloride. The NaCl concentrations were set at 0, 2, 4, 6, 8, 10, and 12 wt%. To further simulate reservoir conditions, solutions of FG-NCDs-L16 and TA-NCDs-L16 (0.5 g/L) were prepared using formation water. Two experimental protocols were employed. (i) Interfacial tension between the formation water-based NCD solutions and DY crude oil was directly measured at different temperatures (50, 60, 70, 80, and 90 °C). (ii) The same solutions were aged at 80 °C for varying durations (0, 24, 72, 120, 168, and 240 h), after which their interfacial tension with DY crude oil was measured at 80 °C. All tests were performed in triplicate under identical conditions, and the average values were reported.

2.4.4. Core flooding experiments

FG-NCDs-L12, FG-NCDs-L16, TA-NCDs-L12, and TA-NCDs-L16 were each dissolved in 8 wt% NaCl solution to prepare 0.5 g/L surfactant-brine flooding solutions for core flooding experiments (see Fig. 2). The physical parameters of the cores are summarized in Table S1. First, the cores were saturated with 8 wt% NaCl solution and then flooded with DY crude oil at a constant flow rate of 0.02 mL/min until the brine was completely displaced. The oil-saturated cores were then aged at 60 °C for 120 h to establish a naturally oil-wet state. The flooding test consisted of three stages. In the first stage (initial water flooding), the cores were flooded with 8 wt% NaCl solution at a constant flow rate of 0.1 mL/min until the injection pressure stabilized and no oil was observed in the effluent. The volume of displaced oil and the injection pressure were recorded. In the second stage (chemical flooding), after releasing the pressure, the biomass-derived amphiphilic NCD surfactant-brine solutions were injected with a total volume equivalent to three times the pore volume (PV) of the core. During this stage, the oil production and injection pressure were monitored. In the third stage (subsequent water flooding), the cores were left undisturbed for 24 h. After pressure release, a second round of water flooding with 8 wt% NaCl solution was performed under the same flow rate until the pressure stabilized and no further oil was recovered. Additionally, 0.5 g/L solutions of FG-NCDs-L16 and TA-NCDs-L16 were prepared using formation water instead of brine, and core flooding experiments were conducted at different temperatures (50, 60, 70, 80, and 90 °C) following the same procedures to simulate reservoir conditions. Each flooding experiment was conducted in triplicate under identical conditions, and average values were reported. The oil recovery (OR), EOR, and pressure reduction rate (PR) were calculated using the following equations:

$$\mathrm{OR} = (V_1 + V_2 + V_3) / V_0 \times 100\% \tag{1}$$

$$\mathrm{EOR} = (V_2 + V_3) / V_0 \times 100\% \tag{2}$$

$$\mathrm{PR} = (P_1 - P_3) / P_1 \times 100\% \tag{3}$$

where V_1 is the oil volume recovered during the initial water flooding, mL; V_2 is the oil volume recovered during chemical flooding, mL; V_3 is the oil volume recovered during subsequent water flooding, mL; and V_0 is the original oil saturation volume in the core, mL; P_1 and P_3 represent the stabilized injection pressures after the initial and subsequent water flooding stages, respectively, MPa.

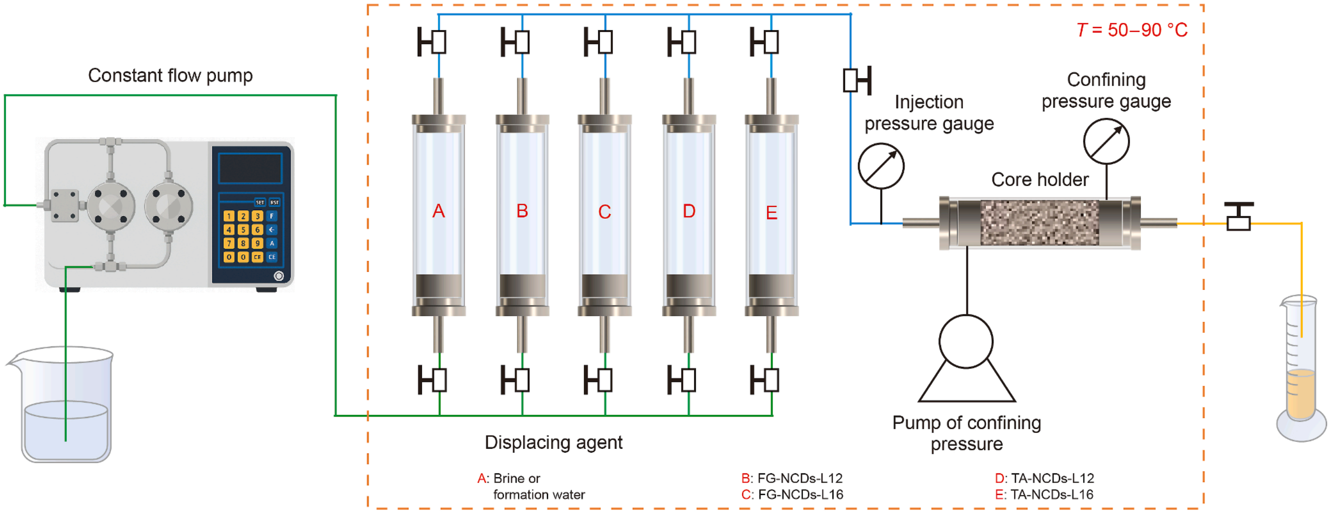

Fig. 2. Schematic diagram of the core flooding setup for evaluating oil displacement efficiency under controlled injection conditions.

3. Results and discussion

3.1. Structural analysis of amphiphilic NCDs

The morphology of six synthesized carbon dot samples, including FG-NCDs, FG-NCDs-L12, FG-NCDs-L16, TA-NCDs, TA-NCDs-L12, and TA-NCDs-L16, was characterized by TEM, as shown in Fig. 3. As observed in Fig. 3(a)–(f), all samples exhibited quasi-spherical morphology with uniform dispersion, and no apparent aggregation was detected, indicating excellent dispersibility of the synthesized carbon dot systems. High-resolution TEM (HRTEM) images revealed distinct lattice fringes in each sample, with an interplanar spacing of approximately 0.20 nm. This value corresponds to the (100) plane of graphitic carbon, suggesting that the carbon dots possess a graphitic-like core structure (Ren et al., 2022). The particle sizes of 100 randomly selected carbon dots per sample were measured using Nano Measure software. The statistical results (Fig. 3(a2)–(f2)) showed relatively narrow size distributions, approximately following Gaussian profiles, with no significant tailing toward larger sizes. This indicates that both the synthesis and purification processes provided good control over size uniformity. A comparison of the average particle sizes revealed that for the FG series, the diameter increased from 2.67±0.55 nm for the unmodified sample to 3.35±0.57 nm after quaternary-ammonium and alkyl chain modification. Similarly, the TA series showed a size increase from 3.30±0.72 nm to 3.99±0.73 nm with increasing chain length. Given the absence of aggregation observed in TEM images and the size increase with longer alkyl chains, it is inferred that the increase in particle size primarily results from the contribution of the organic shell formed by surface alkyl chain modification (Wu et al., 2025a). A further comparison between the two series revealed that the TA-based carbon dots exhibited larger particle sizes than the FG-based counterparts under the same alkyl chain conditions. This difference is likely related to the molecular structure of the precursors. Tartaric acid, the precursor of the TA series, contains two carboxyl groups, which provide a higher density of reactive sites for amidation. As a result, more quaternary ammonium groups and hydrophobic chains are grafted onto the surface, leading to a larger overall size compared with the FG series derived from fenugreek gum.

The surface functional groups and structural differences of the six carbon dot samples were further analyzed using FT-IR spectroscopy. As shown in Fig. 4, all samples exhibited a broad and intense absorption band centered around 3291 cm^{-1}, which can be attributed to the stretching vibrations of hydroxyl and amino groups (O–H and N–H) (Yang et al., 2023). This indicates that polar oxygen- and nitrogen-containing groups were partially retained after the carbonization and nitrogen-doping processes of both precursor types. In the region of 2960–2850 cm^{-1}, multiple characteristic peaks corresponding to the asymmetric and symmetric stretching vibrations of $-CH_3$ and $-CH_2-$ groups were observed (Lu et al., 2024). These peaks are indicative of the successful incorporation of long-chain alkyl groups. As the alkyl chain length increased from L12 to L16, the intensity of these peaks also increased, confirming the progressive enrichment of hydrophobic segments on the carbon dot surfaces. In the region of 1770–1650 cm^{-1}, several absorption peaks corresponding to carbonyl-containing groups were detected. For the TA-based samples (Fig. 4(b)), distinct C=O stretching peaks appeared at 1770 and 1707 cm^{-1}, which are characteristic of carboxylic acid carbonyl groups (Ye et al., 2020). In contrast, the FG-based samples (Fig. 4(a)) showed only a weak shoulder peak around 1698 cm^{-1}, suggesting a significantly lower content of residual carboxyl groups. This difference is closely related to the molecular structures of the precursors. Fenugreek gum is a natural polysaccharide rich in hydroxyl groups and acetal linkages. During solvothermal treatment, it undergoes oxidation, dehydration, and bond rearrangement, generating only a limited number of carboxyl groups. On the other hand, tartaric acid is inherently rich in dicarboxyl groups, which are more likely to be preserved during carbonization, resulting in a higher surface carboxyl group density in the TA-NCDs. This structural feature may also lead to differences in the extent of subsequent amidation and quaternization. Both the FG and TA series showed strong absorption bands at 1654 cm^{-1}, which can be assigned to the amide I band (C=O stretching) or the stretching vibration of *sp*^{2} carbon frameworks (C=C) (Wu et al., 2025a). The absorption observed in the 1530–1540 cm^{-1} region corresponds to the amide II band (N–H bending) (Zhu et al., 2021) or the stretching vibration of quaternary ammonium $C-N^+$ bonds (Tan et al., 2011). In the range of 1460–1370 cm^{-1}, all samples exhibited bending vibrations of $-CH_3$ and $-CH_2-$ groups (Ding et al., 2009), with increasing intensity observed for samples modified with longer alkyl chains. This further supports the successful surface functionalization with alkyl groups. Additionally, strong absorption bands were observed in the 1088 and 1046 cm^{-1} region

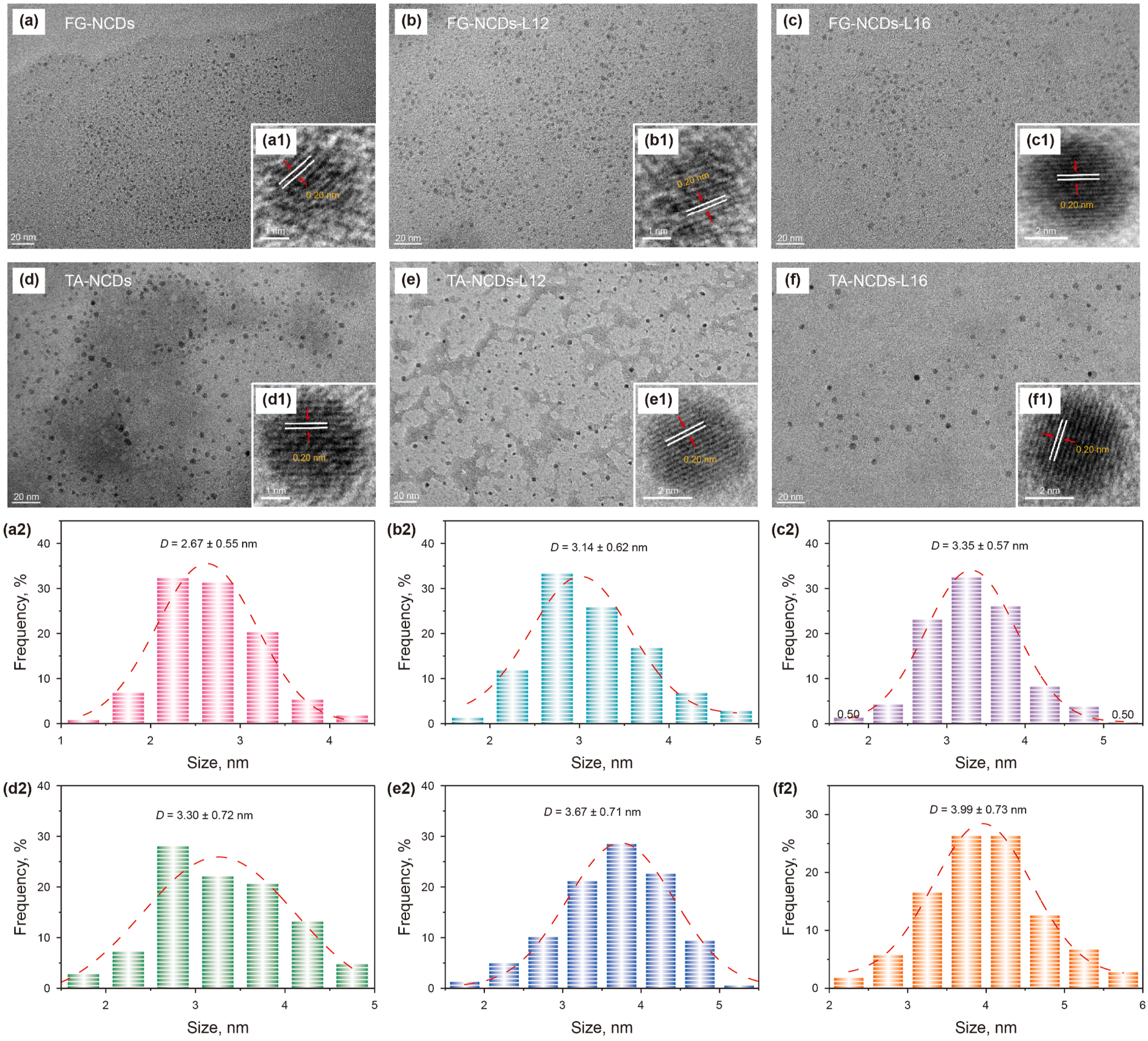

Fig. 3. TEM images, HRTEM images, and particle size distributions of FG-NCDs (**a, a1**, **a2**), FG-NCDs-L12 (**b**, **b1**, **b2**), FG-NCDs-L16 (**c**, **c1**, **c2**), TA-NCDs (**d**, **d1**, **d2**), TA-NCDs-L12 (**e**, **e1**, **e2**), and TA-NCDs-L16 (**f**, **f1**, **f2**).

for all samples, which are attributed to the symmetric and asymmetric stretching vibrations of C–O or C–N bonds (Zhang et al., 2022). The enhanced absorption in this region for modified samples may be related to the presence of ether bonds along the alkyl chains and the increased density of quaternary ammonium groups. Moreover, a pronounced absorption near 880 cm^{-1} was detected in the modified samples, corresponding to the N^{+}–CH$_3$ stretching vibration, confirming the successful introduction of quaternary ammonium cations on the carbon dot surfaces (Delgado-Mellado et al., 2018).

To further investigate the elemental composition and chemical states on the surface of the carbon dots, XPS analysis was conducted, and the results are shown in Fig. 5 and Table S2. As illustrated in the survey spectra (Fig. 5(a) and (b)), all samples primarily consist of carbon (C), nitrogen (N), and oxygen (O). Trace amounts of chlorine (Cl) were detected in the alkyl-modified samples, originating from the incorporation of the linking groups. Compared with the unmodified samples, both FG- and TA-based carbon dots showed a noticeable increase in carbon content and a corresponding decrease in oxygen content after alkyl chain modification. This trend reflects the successful introduction of hydrophobic alkyl segments on the surface, which reduced the relative proportion of hydrophilic oxygen-containing groups. In addition, TA-NCDs exhibited a higher nitrogen content than FG-NCDs. This observation supports the conclusion that tartaric acid, due to its abundant carboxyl groups, provided more reactive sites for amidation, thereby enhancing the nitrogen incorporation during surface functionalization.

The high-resolution C 1*s* spectra provide insights into the surface carbon bonding configurations of the carbon dots. In FG-NCDs (Fig. 5(a1)), the peaks corresponding to C–C/C=C (284.8 eV) (Ye et al., 2020) and C–O/C–N (286.0 eV) (Wu et al., 2025b) accounted for 58.01% and 32.33% of the total carbon signal, respectively, while the C=O component (287.7 eV) (Xu et al., 2023) contributed

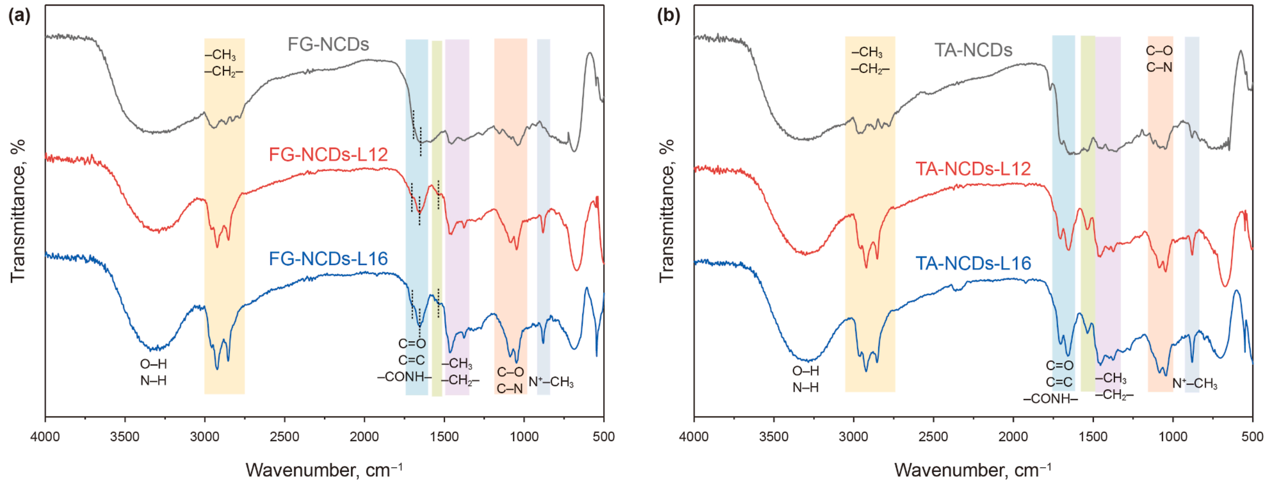

Fig. 4. FT-IR spectra of synthesized NCDs: (**a**) FG-NCDs, FG-NCDs-L12, FG-NCDs-L16; (**b**) TA-NCDs, TA-NCDs-L12, TA-NCDs-L16.

only 9.66%. In contrast, TA-NCDs (Fig. 5(b1)) exhibited a higher proportion of C–O/C–N (43.27%) and an increased C=O contribution (14.48%), indicating a significant enrichment of oxygen-containing carbonyl and nitrogen-containing functional groups on the surface of the TA-based carbon dots. Upon quaternization and alkyl chain functionalization, the relative intensity of C–C/C=C peaks increased markedly, while both C–O/C–N and C=O components decreased in both series of carbon dots. This trend confirms the successful grafting of hydrophobic alkyl segments and their substantial impact on the surface bonding composition. The high-resolution N 1*s* spectra further reveal the nitrogen bonding environments. All samples exhibited characteristic peaks associated with pyridinic N (around 399 eV), pyrrolic N/–NH– (around 400 eV), and graphitic N (in the range of 401–402 eV), indicating the formation of multiple nitrogen-doping configurations during the carbonization and doping processes (Ding et al., 2014; Liu et al., 2024). After alkyl chain modification, a new signal corresponding to quaternary ammonium nitrogen (N$^+$–(C$_4$), 402.3 eV) (Li et al., 2023b) appeared and showed a significant increase in intensity. The relative content of this component reached 21.63% and 26.23% in FG-NCDs-L12 (Fig. 5(a4)) and FG-NCDs-L16 (Fig. 5(a6)), respectively, and further increased to 27.21% and 34.46% in TA-NCDs-L12 (Fig. 5(b4)) and TA-NCDs-L16 (Fig. 5(b6)), respectively. This trend clearly reflects the influence of precursor structure on carboxyl group density, which determines the number of available activation sites for amidation. Due to the higher carboxyl group content in tartaric acid, the TA series was able to incorporate a greater number of quaternary ammonium groups after multi-step modification. This resulted in higher surface charge density and a more pronounced amphiphilic framework. The elevated content of surface quaternary ammonium groups not only enhances electrostatic adsorption at the oil–water interface but also contributes to the formation of more stable interfacial films and improved salt resistance, laying a strong foundation for efficient interfacial regulation under harsh reservoir conditions.

UV–Vis and PL spectroscopy were further employed to investigate the structural characteristics and optical properties of the carbon dots. The results are presented in Fig. 6. As shown in the UV–Vis spectra (Fig. 6(a)–(f)), all carbon dot samples exhibited three characteristic absorption peaks. A strong absorption band around 200 nm is attributed to π–π* transitions of C=C conjugated domains. A shoulder peak at approximately 273–276 nm corresponds to n–π* transitions related to surface nitrogen-containing heterocycles. A weaker shoulder near 330–335 nm is associated with n–π* transitions originating from oxygen-containing functional groups or surface defect states (Li et al., 2023a; Pan et al., 2021). For the FG-based carbon dots, the intensities of all three absorption features decreased significantly after alkyl chain modification. Among them, FG-NCDs-L16 exhibited the weakest absorption. This reduction may be attributed to the grafted hydrophobic alkyl chains partially covering the surface active sites, thereby limiting the exposure of heteroatoms and related defect states and suppressing the corresponding electronic transitions. In comparison, the TA-based carbon dots showed generally stronger UV absorption, which is likely due to the higher carboxyl group content in the tartaric acid precursor. This structural feature promotes more extensive heteroatom doping and defect formation on the carbon dot surface, resulting in a greater number of n–π* transition sites.

The PL spectra further revealed the excitation-dependent emission behavior of the carbon dots. For FG-NCDs (Fig. 6(a)), the emission peak gradually red-shifted from 416 to 462 nm as the excitation wavelength increased from 320 to 400 nm. The corresponding fluorescence intensity first increased and then decreased, reaching a maximum at an excitation wavelength of 360 nm. After alkyl chain modification, FG-NCDs-L12 (Fig. 6(b)) and FG-NCDs-L16 (Fig. 6(c)) exhibited further red-shifted emission peaks, with maximum emission observed up to 463 nm. However, their fluorescence intensities were significantly reduced. The emission intensity of FG-NCDs-L16, which contains a longer alkyl chain, decreased more sharply. This trend indicates that the increasing length of the hydrophobic alkyl chains led to progressive shielding of surface heteroatom sites and defect states, thereby reducing emission intensity and inducing red-shifted fluorescence peaks. Compared with the FG series, the TA-based carbon dots displayed markedly enhanced fluorescence performance. For instance, TA-NCDs (Fig. 6(d)) showed a much higher maximum emission intensity under 360 nm excitation than FG-NCDs, with an emission wavelength range of 415–461 nm. Similar to the FG series, TA-NCDs-L12 (Fig. 6(e)) and TA-NCDs-L16 (Fig. 6(f)) also exhibited red-shifted emission peaks and a gradual reduction in intensity upon alkyl chain modification. However, their fluorescence intensities remained consistently higher than those of the corresponding FG-based samples. This difference in fluorescence behavior further supports the conclusion that the higher carboxyl group content in tartaric acid precursors facilitates the formation of a greater density of heteroatom dopants and defect states during the solvothermal process, leading to higher

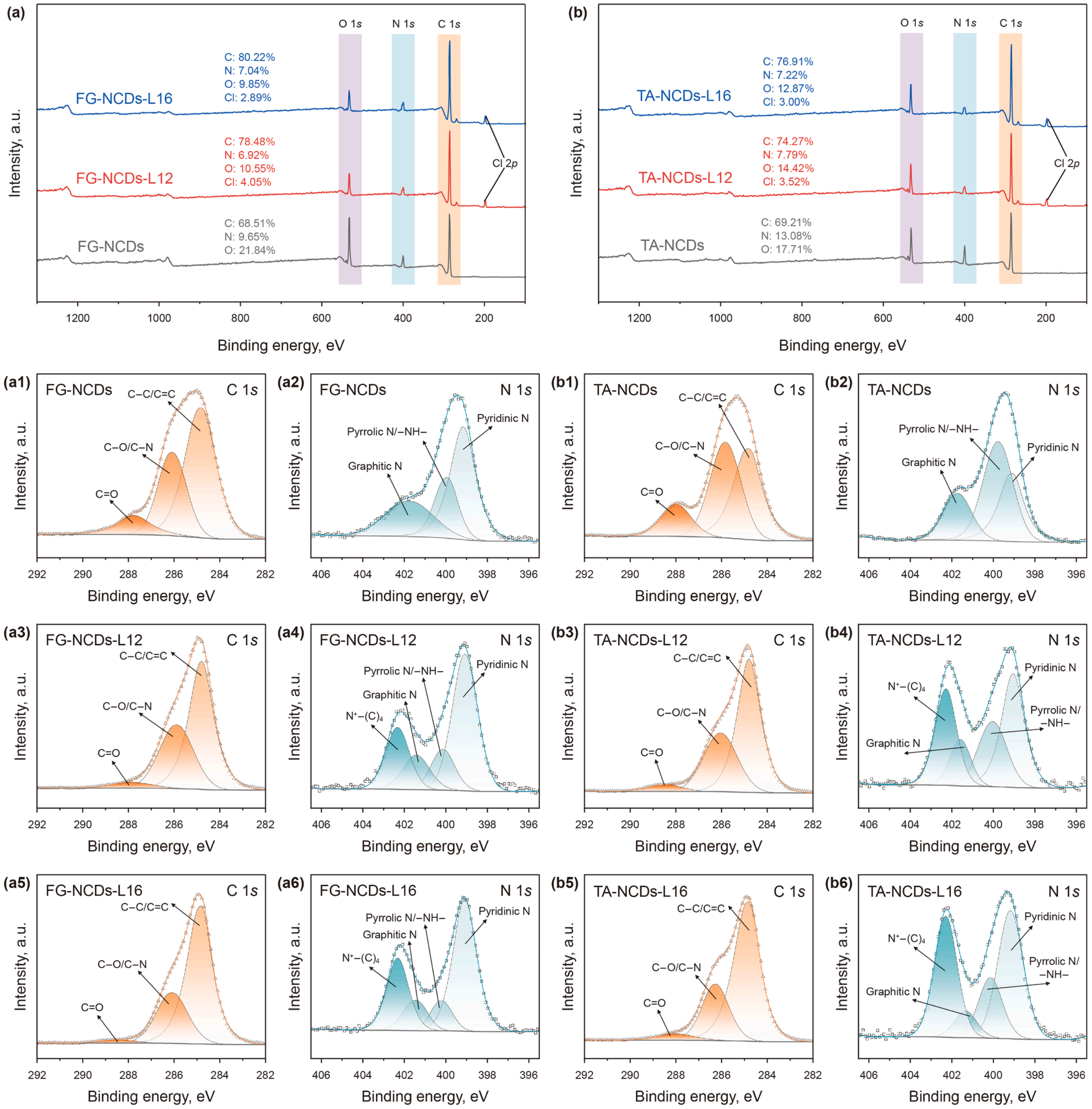

Fig. 5. XPS spectra of synthesized NCDs: survey spectra of FG-series NCDs (**a**) and TA-series NCDs (**b**); high-resolution C 1*s* and N 1*s* spectra of FG-NCDs (**a1**, **a2**), FG-NCDs-L12 (**a3**, **a4**), FG-NCDs-L16 (**a5**, **a6**), TA-NCDs (**b1**, **b2**), TA-NCDs-L12 (**b3**, **b4**), and TA-NCDs-L16 (**b5**, **b6**).

fluorescence intensity (Wu et al., 2025b). Although the introduction of hydrophobic chains also suppresses fluorescence emission in the TA series, the overall emission intensity remains superior due to the significantly higher density of surface functional groups and defect sites.

3.2. Surface/interfacial performance of amphiphilic NCDs

3.2.1. Surface tension and micellization behavior

To elucidate the interfacial activity of FG-NCDs and TA-NCDs after alkyl chain modification (L12 and L16), the surface tension (γ) of the carbon dot solutions was measured as a function of concentration (C), as shown in Fig. 7. All carbon dots exhibited typical surfactant-like γ–C curves, characterized by an initial sharp decrease in surface tension followed by a gradual plateau. The CMC and the corresponding γ value (γ_{CMC}) were determined by linear fitting of the surface tension curves (Li et al., 2019).

In the FG series (Fig. 7(a)), unmodified FG-NCDs displayed the highest CMC value (0.662 g/L) and the highest γ_{CMC} (48.52 mN/m), indicating limited interfacial activity at the air–liquid interface. After alkyl chain modification, the interfacial activity was significantly enhanced. The CMC values of FG-NCDs-L12 and FG-NCDs-L16 decreased to 0.539 and 0.328 g/L, respectively, with corresponding γ_{CMC} values reduced to 28.35 and 27.85 mN/m. The

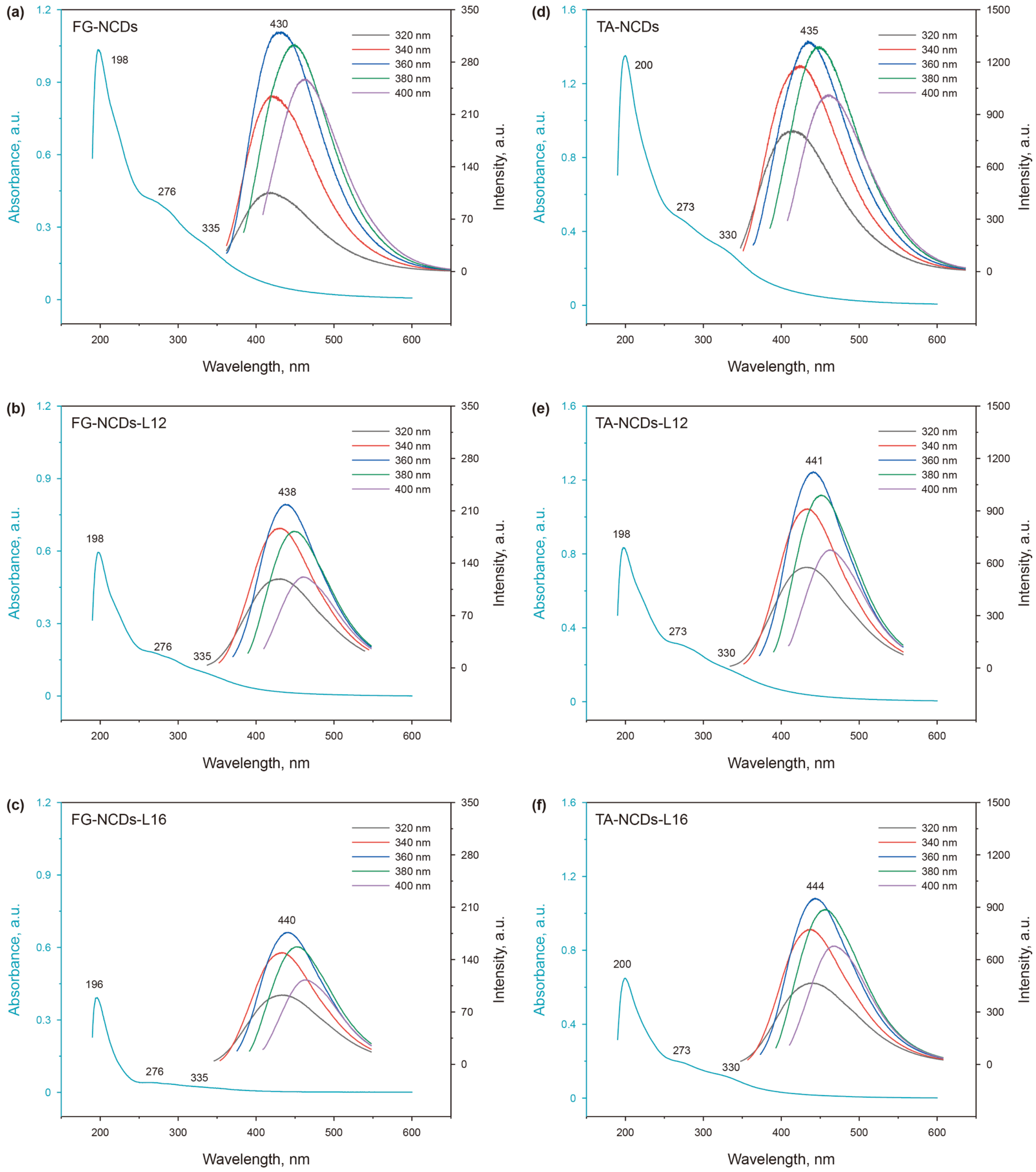

Fig. 6. UV–Vis and PL spectra for synthesized NCDs: (**a**) FG-NCDs; (**b**) FG-NCDs-L12; (**c**) FG-NCDs-L16; (**d**) TA-NCDs; (**e**) TA-NCDs-L12; (**f**) TA-NCDs-L16.

introduction of both alkyl chains and quaternary ammonium groups increased the overall hydrophobicity and amphiphilic character of the carbon dots, thereby enhancing their spontaneous adsorption at the air–liquid interface and effectively reducing the surface tension (Sharma et al., 2016). In comparison, the TA-based carbon dots (Fig. 7(b)) exhibited overall superior interfacial activity. The unmodified TA-NCDs showed a lower CMC value (0.523 g/L) than FG-NCDs, indicating a stronger tendency for micelle formation in solution. However, its γ_{CMC} value (49.71 mN/m) was slightly higher than that of FG-NCDs, suggesting a slightly weaker maximum adsorption capacity at the interface. Upon alkyl modification, the CMC values of TA-NCDs-L12 and TA-NCDs-L16 further decreased to 0.189 and 0.104 g/L, respectively, while their γ_{CMC} values dropped to 25.87 and 24.71 mN/m. These results were markedly better than those of the corresponding FG-based samples.

The superior performance of the TA series is attributed to the higher density of carboxyl groups in tartaric acid, which provides

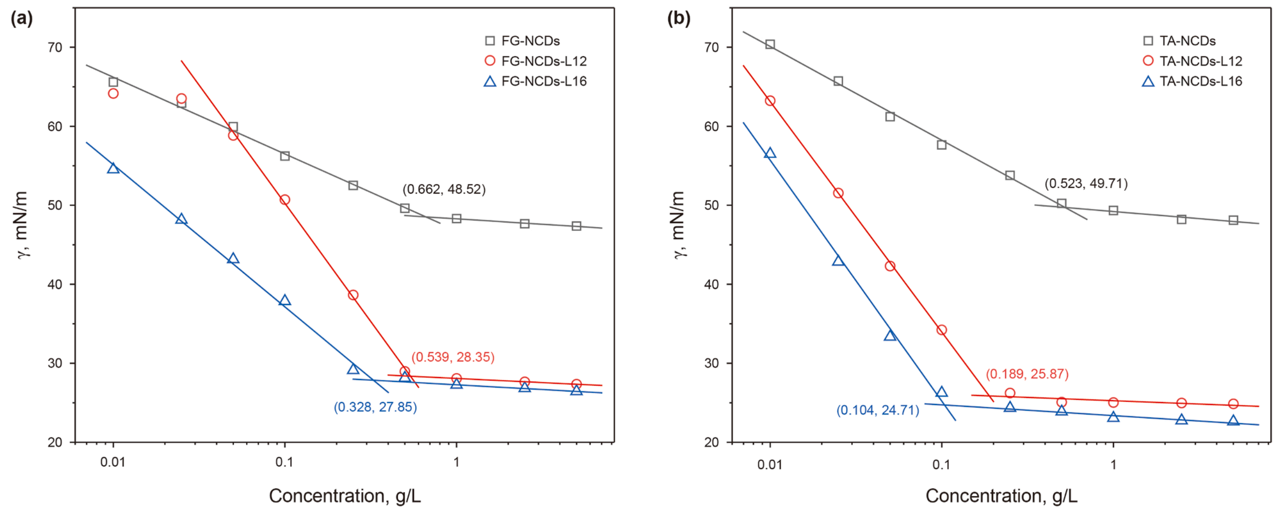

Fig. 7. Surface tension curves of synthesized NCDs as a function of concentration: (**a**) FG-NCDs, FG-NCDs-L12, FG-NCDs-L16; (**b**) TA-NCDs, TA-NCDs-L12, TA-NCDs-L16.

more active sites for amidation, quaternization, and alkylation. This results in a greater number of surface-grafted hydrophilic quaternary ammonium groups and hydrophobic alkyl chains, thereby enhancing amphiphilicity and interfacial adsorption capacity. The lower CMC values suggest that surface saturation can be achieved at lower concentrations, facilitating the formation of densely packed interfacial films. Additionally, both series exhibited a clear chain length effect. Samples modified with L16 consistently showed lower CMC and γ_{CMC} values compared to those modified with L12. This indicates that longer alkyl chains promote the formation of more stable and ordered interfacial assemblies due to stronger hydrophobic interactions within the molecular structure.

The self-assembly behavior and micelle formation characteristics of the four biomass-derived amphiphilic NCDs were systematically investigated by dynamic light scattering (DLS), which was used to monitor the evolution of hydrodynamic diameter at various concentrations (Fig. 8). Overall, all samples exhibited a typical concentration-dependent increase in particle size, accompanied by a gradual transition from unimodal to bimodal size distributions across the concentration range.

At low concentrations (0.01 and 0.05 g/L), nearly all amphiphilic NCD systems displayed narrow, unimodal distributions with average particle sizes ranging from 5 to 16 nm. These values were close to the original particle sizes observed in TEM images, indicating that the carbon dots primarily existed in the form of dispersed monomers or small oligomers, with no significant self-assembly occurring at this stage. As the concentration increased to 0.1 g/L, all samples exhibited a shift toward bimodal distributions, indicating the onset of concentration-induced self-assembly and the formation of micelles or large pre-micellar aggregates. For example, FG-NCDs-L16 exhibited a major aggregate peak at 164.18 nm and an average hydrodynamic diameter of 158.10 nm at 0.1 g/L. In comparison, TA-NCDs-L16 showed a larger aggregate peak at 255.00 nm, with an average size of 197.14 nm, suggesting that the TA-based carbon dots tended to form larger aggregates at lower concentrations. At higher concentrations (0.5 and 1 g/L), the size of the aggregates increased significantly. The dominant peaks in the DLS profiles shifted progressively toward larger diameters, reaching several hundred nanometers, confirming enhanced intermolecular self-assembly above the CMC. At 1 g/L, the main aggregate sizes of FG-NCDs-L16 and TA-NCDs-L16 reached 342.00 and 396.06 nm, respectively, with average sizes of 298.37 and 365.73 nm. These results indicate substantial micellar expansion and structural stability under concentration-driven conditions.

This behavior was consistent with the surface tension measurements discussed previously, further confirming that the differences in precursor functional group composition and the degree of quaternization–alkylation play a key role in self-assembly. The higher carboxyl group density provided by the tartaric acid precursor in the TA series enabled the formation of a more highly polarized surface after amidation, quaternization, and alkylation. This promoted stronger intermolecular electrostatic interactions, facilitating the formation of larger and more compact micelles or supramolecular aggregates. In parallel, the presence of long-chain alkyl groups enhanced hydrophobic interactions, stabilizing the micelle cores through efficient hydrophobic domain packing (Suting et al., 2023).

Overall, the combined results of surface tension and DLS measurements highlight the significant influence of alkyl chain length and precursor type on the interfacial activity and self-assembly behavior of the carbon dots. Increasing the alkyl chain length markedly reduced the CMC and enhanced interfacial adsorption capacity. This effect was further amplified in the TA series, where the tartaric acid precursor, rich in carboxyl groups, provided additional functional sites, resulting in superior surface activity and stronger self-assembly ability compared to the FG-based carbon dots. The evolution of hydrodynamic diameter revealed a concentration-dependent and structure-driven self-assembly process. At low concentrations, the carbon dots predominantly existed as monomeric species or small aggregates. In the intermediate concentration range, nucleation and growth of micellar structures became evident. At high concentrations, stable higher-order aggregates were formed, indicating well-developed supramolecular organization. These structure–property relationships not only demonstrate the excellent interfacial self-organization capability of amphiphilic NCDs but also provide a solid foundation for their potential in constructing stable adsorption layers at complex oil–water interfaces. The findings offer both theoretical and experimental support for the future application of these amphiphilic carbon dots in wettability regulation and enhanced oil recovery processes.

3.2.2. pH-responsive behavior

To investigate the pH-dependent interfacial properties and colloidal stability of the biomass-derived amphiphilic NCDs,

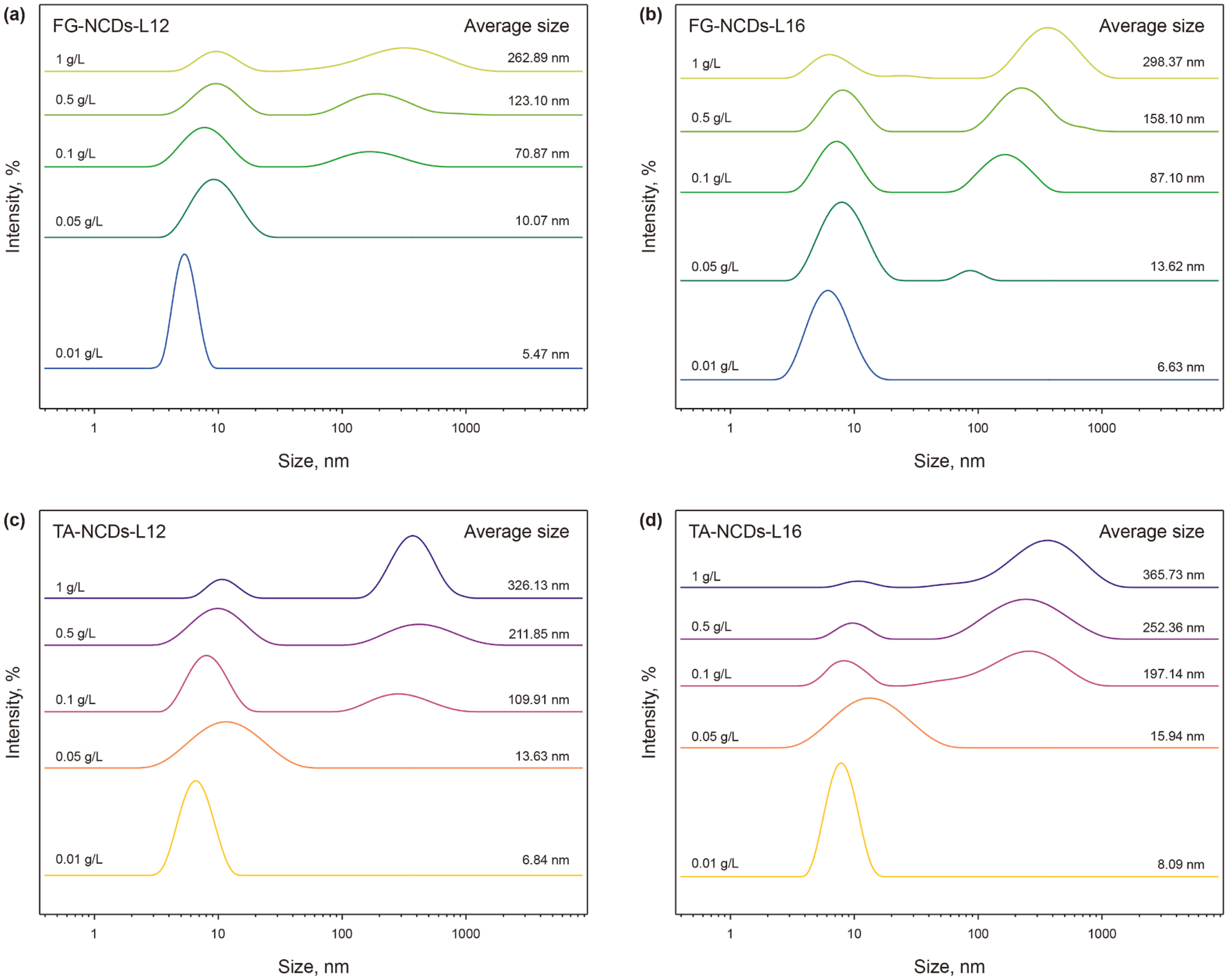

Fig. 8. Size distribution of amphiphilic NCDs as a function of concentration: (**a**) FG-NCDs-L12; (**b**) FG-NCDs-L16; (**c**) TA-NCDs-L12; (**d**) TA-NCDs-L16.

surface tension and zeta potential were measured across a pH range from 1 to 13 (Fig. 9(a) and (b)). All samples exhibited a pronounced U-shaped trend in surface tension as a function of pH. Specifically, surface tension values were higher under strongly acidic and basic conditions but reached their minimum near neutral pH. This indicates that the interfacial adsorption capacity and molecular orientation of the NCDs are strongly influenced by pH. For example, in the FG series, the surface tension of FG-NCDs-L12 and FG-NCDs-L16 decreased to 26.28 and 24.23 mN/m, respectively, at pH 7. Under highly acidic conditions (pH 1), these values increased to 32.97 and 31.23 mN/m, respectively. In comparison, the TA series exhibited even greater interfacial activity. The surface tensions of TA-NCDs-L12 and TA-NCDs-L16 were further reduced to 17.66 and 15.48 mN/m at pH 7, respectively. Moreover, the TA-based samples showed a larger variation in surface tension across the pH range, suggesting a more sensitive interfacial response to environmental pH fluctuations. The zeta potential measurements further supported these findings by providing electrostatic evidence. Zeta potential is a critical indicator of the colloidal stability of nanofluids, as it reflects the magnitude of electrostatic repulsion between particles. In general, systems with zeta potentials higher than +30 mV or lower than −30 mV are considered electrostatically stable (Cao et al., 2023b). All four samples maintained a positive surface charge across the entire pH range, indicating that the quaternary ammonium groups remained dominant in determining surface charge characteristics. As the pH increased, the zeta potential initially increased and then decreased, with peak values occurring near neutral pH. For instance, FG-NCDs-L16 reached a maximum of +44.03 mV at pH 7, while TA-NCDs-L16 reached as high as +67.80 mV. Throughout the entire pH range, the TA-based carbon dots exhibited consistently higher zeta potentials than the FG-based samples, confirming that their higher density of quaternary ammonium groups contributed to stronger surface charge and enhanced colloidal stability.

The observed pH-responsive behavior in surface tension and zeta potential is fundamentally attributed to the complex cooperative regulation of the multi-functional surface chemistry of the carbon dots at the electrostatic level. Quaternary ammonium cations, as permanent positively charged centers, theoretically retain a constant charge across the entire pH range. In contrast, residual surface carboxyl groups act as pH-responsive sites, modulating local interfacial charge balance and polarity through protonation and deprotonation processes. Under strongly acidic conditions (pH 1–3), the carboxyl groups are fully protonated, eliminating their negative charge contribution. However, the high concentration of H^+ ions leads to significant compression of the electrical double layer, enhancing counterion shielding around the quaternary ammonium groups and resulting in a reduced zeta potential. Meanwhile, disruption of hydration shell structures at low pH interferes with the molecular alignment at the interface, thereby increasing surface tension. At high pH values (pH 11–13),

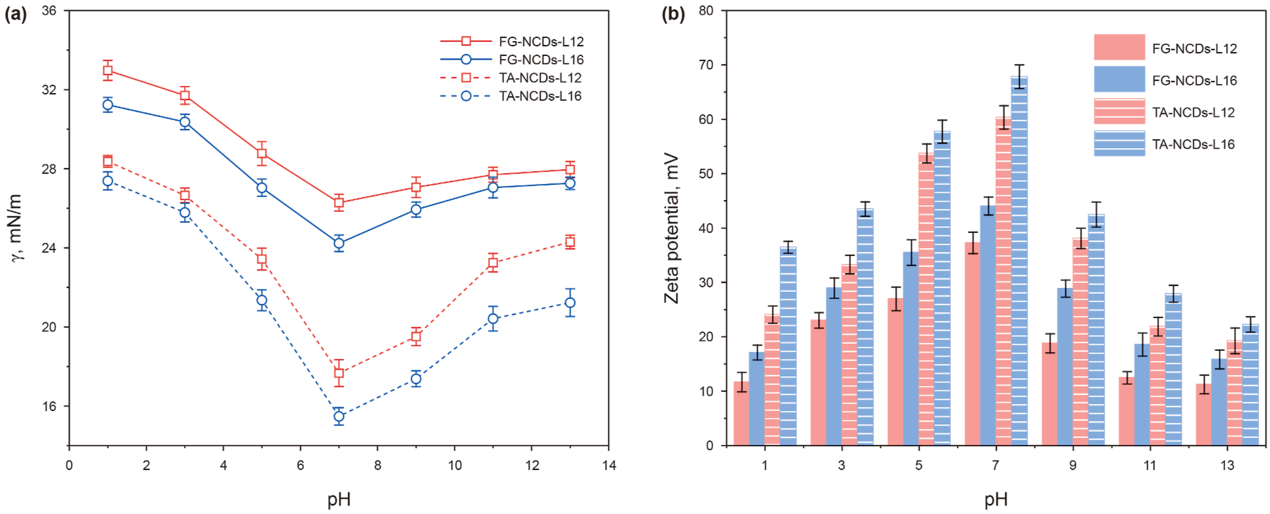

Fig. 9. Surface tension (**a**) and zeta potential (**b**) of amphiphilic NCDs as a function of pH.

carboxyl groups are fully deprotonated into carboxylate anions, increasing the density of negative charges. These negatively charged sites partially compensate for the fixed positive charges of the quaternary ammonium groups, which diminishes the net surface charge expression. Consequently, a decrease in zeta potential and a corresponding increase in surface tension are also observed in alkaline environments. Near neutral pH, the carboxyl groups exist in a dynamic equilibrium between protonated and deprotonated states. This balance results in an optimal distribution of counterions, which supports efficient electrostatic shielding, favorable polarity–hydrophobicity interactions, and enhanced molecular ordering at the interface. As a result, the interfacial adsorption layer is most compact and well-structured under neutral conditions, yielding the lowest surface tension and the highest zeta potential.

In summary, the surface interfacial adsorption behavior and colloidal stability of the carbon dots under varying pH conditions were jointly regulated by the density of quaternary ammonium groups and the length of the hydrophobic alkyl chains. In the TA series, the presence of dicarboxylic structures in the tartaric acid precursor provided abundant reactive sites for amidation and subsequent quaternization, leading to a higher density of polar cationic groups and hydrophobic chains. This resulted in a more ordered and balanced distribution of polar and non-polar units within the interfacial framework. Moreover, the introduction of long alkyl chains, such as L16, further enhanced the directional adsorption and ordered arrangement of the carbon dots at the interface. This contributed to superior surface activity and electrostatic stability across a wide pH range (Shahan et al., 2017). The structural advantages arising from the synergy between high quaternary ammonium density and flexible hydrophobic chain segments endowed the TA-based carbon dots with excellent pH-responsive interfacial regulation capabilities and colloidal stability. These features provide a solid molecular basis and strong environmental adaptability for their potential application in interfacial control under complex reservoir conditions.

3.2.3. *Contact angle and wettability*

To evaluate the wettability reversal capability of the biomass-derived amphiphilic NCDs on hydrophobic surfaces, a combined approach involving static adsorption and dynamic contact angle measurement was employed to assess the interfacial behavior of the polar modification layers formed by the carbon dots. As shown in Fig. 10, all samples exhibited effective wettability reversal performance. With increasing NCD solution concentration, the surface coverage of carbon dot molecules and the exposure of polar functional groups in the adsorbed layer gradually increased. This led to a continuous decrease in the water contact angle, indicating a significant enhancement in surface wettability (Wang et al., 2023).

In the FG series, FG-NCDs-L12 (Fig. 10(a)) and FG-NCDs-L16 (Fig. 10(b)) reduced the final contact angle to 59.65° and 49.16°, respectively, at a concentration of 1 g/L. In contrast, the TA-based samples exhibited more pronounced wettability reversal. Under the same conditions, TA-NCDs-L12 (Fig. 10(c)) and TA-NCDs-L16 (Fig. 10(d)) further decreased the contact angle to 36.76° and 16.30°, respectively, approaching a fully hydrophilic state. The inset images depicting droplet shape changes provided additional visual confirmation of the substantial wettability transition. These differences highlight the synergistic effect between polar group density and hydrophobic chain length in the amphiphilic molecular structure of the carbon dots. The tartaric acid precursor in the TA series provided a high density of reactive carboxyl groups, which, upon amidation and efficient quaternization, generated abundant cationic polar centers. Meanwhile, the long alkyl chains enhanced the hydrophobic interaction with the surface, promoting stable adsorption and dense molecular packing at the hydrophobic interface (Bao et al., 2024; Li et al., 2018b). The dynamic contact angle measurements further revealed interfacial reorganization and polarity optimization during the interaction between the adsorbed film and the water droplet. Most samples exhibited a rapid initial decrease in contact angle, followed by gradual stabilization, indicating a two-stage process. In the initial stage, polar functional groups in the adsorption layer rapidly formed hydrogen bonds and dipolar interactions with the water phase. This was accompanied by minor molecular rearrangement and interfacial reorganization, ultimately leading to the formation of a stable wetting structure. This effect was particularly evident in samples with highly polar and densely packed interfacial layers. For example, in TA-NCDs-L16 at 1 g/L, the contact angle rapidly decreased from 43.98° to 23.87° within just 20 s, eventually stabilizing at 16.30°. This result demonstrates the excellent wetting responsiveness and interfacial stability of the TA-based carbon dots.

Fundamentally, the excellent wettability reversal performance of the TA-based amphiphilic NCDs on hydrophobic surfaces can be

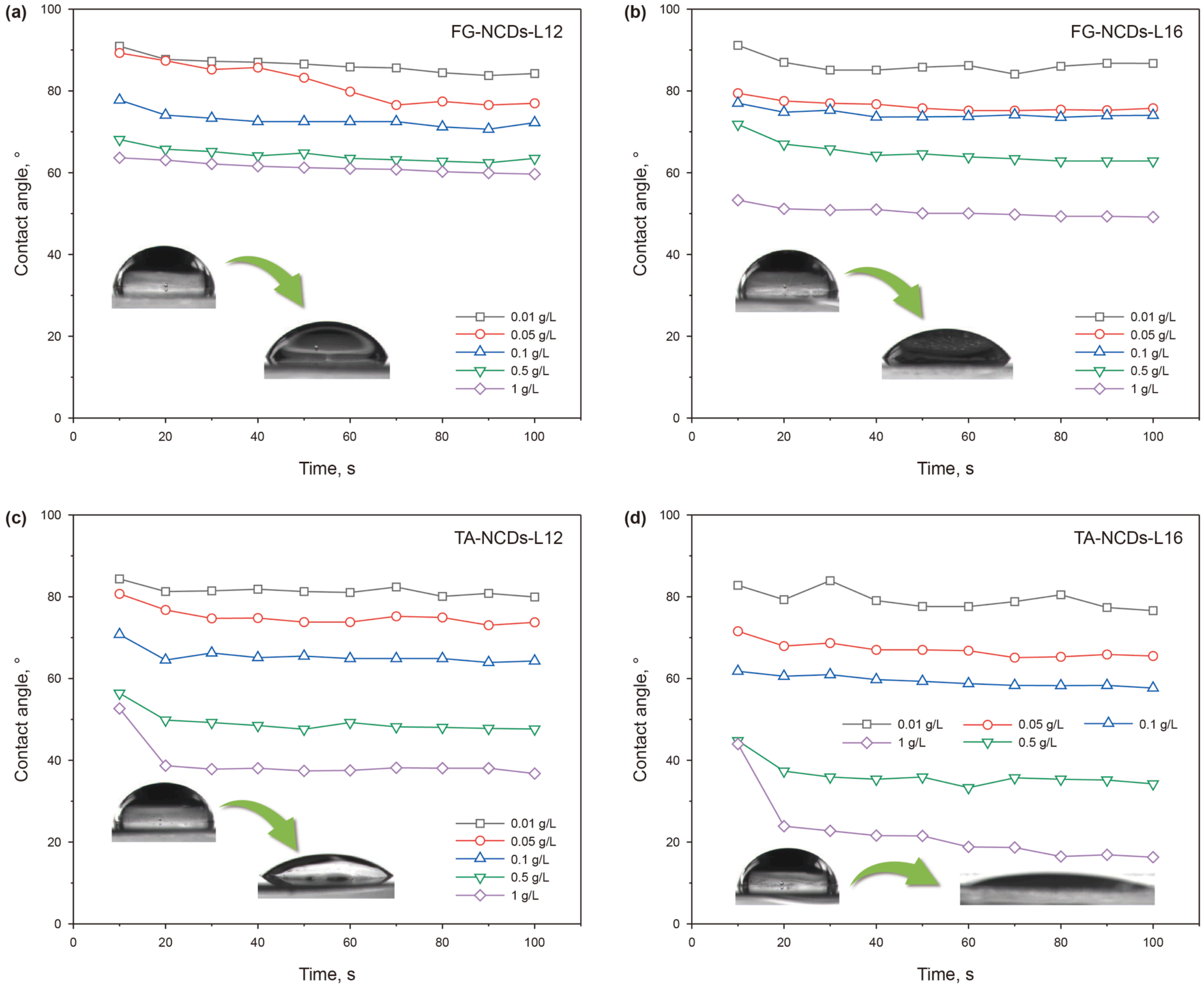

Fig. 10. Water contact angles on silicone oil-coated glass slides after 24 h immersion in amphiphilic NCD solutions of different concentrations (the insets show a comparison of the final droplet shapes at amphiphilic NCD solution concentrations of 0.01 and 1 g/L): (**a**) FG-NCDs-L12; (**b**) FG-NCDs-L16; (**c**) TA-NCDs-L12; (**d**) TA-NCDs-L16.

attributed to the synergistic regulation of surface polar group density, hydrophobic chain length, and molecular spatial configuration. The high density of quaternary ammonium cations enhances the polar driving force, while the long alkyl chains promote hydrophobic–hydrophobic adsorption stability. Moreover, the ordered distribution of polar and non-polar segments facilitates the outward orientation of polar moieties, maximizing their exposure at the interface, reducing interfacial free energy, and ultimately enabling efficient wettability conversion. This interfacial transformation behavior not only demonstrates the superior interfacial regulation potential of the TA-based carbon dots, but also provides a molecular-level explanation for their applicability in wettability alteration and oil–water detachment during oil recovery. The polar adsorption layer formed during the static adsorption stage is expected to reduce oil–rock adhesion in subsequent secondary water flooding, thereby improving oil displacement efficiency and contributing to enhanced recovery performance of the flooding system.

3.2.4. Oil–water interfacial tension and salt responsiveness

Fig. 11 presents a detailed analysis of the oil–water interfacial tension characteristics between four biomass-derived amphiphilic NCD solutions and two types of oil phases (white oil and DY crude oil), as well as their responses to concentration and salinity. Overall, all samples exhibited pronounced concentration-dependent interfacial behavior, with the TA-series carbon dots consistently outperforming their FG-series counterparts. Furthermore, long-chain alkyl modification (L16) showed superior interfacial activity compared to short-chain modification (L12), further underscoring the strong correlation between molecular structure and interfacial performance.

Under salt-free conditions (Fig. 11(a) and (b)), the interfacial tension continuously decreased with increasing NCD concentration from 0.01 to 1 g/L and gradually approached a plateau, indicating a typical concentration-dependent interfacial adsorption saturation behavior. In the white oil system, the minimum interfacial tensions of FG-NCDs-L12 and FG-NCDs-L16 were reduced to 0.24799 and 0.19891 mN/m, respectively, while that of TA-NCDs-L12 and TA-NCDs-L16 further decreased to 0.09866 and 0.04879 mN/m. By comparison, significantly lower interfacial tensions were observed in the DY crude oil system, with TA-NCDs-L16 achieving a minimum value of 0.02619 mN/m at 1 g/L. This variation between oil types primarily arises from the compositional differences between white oil and DY crude oil. White oil consists almost entirely of saturated hydrocarbons, making the interfacial behavior highly dependent on the molecular adsorption

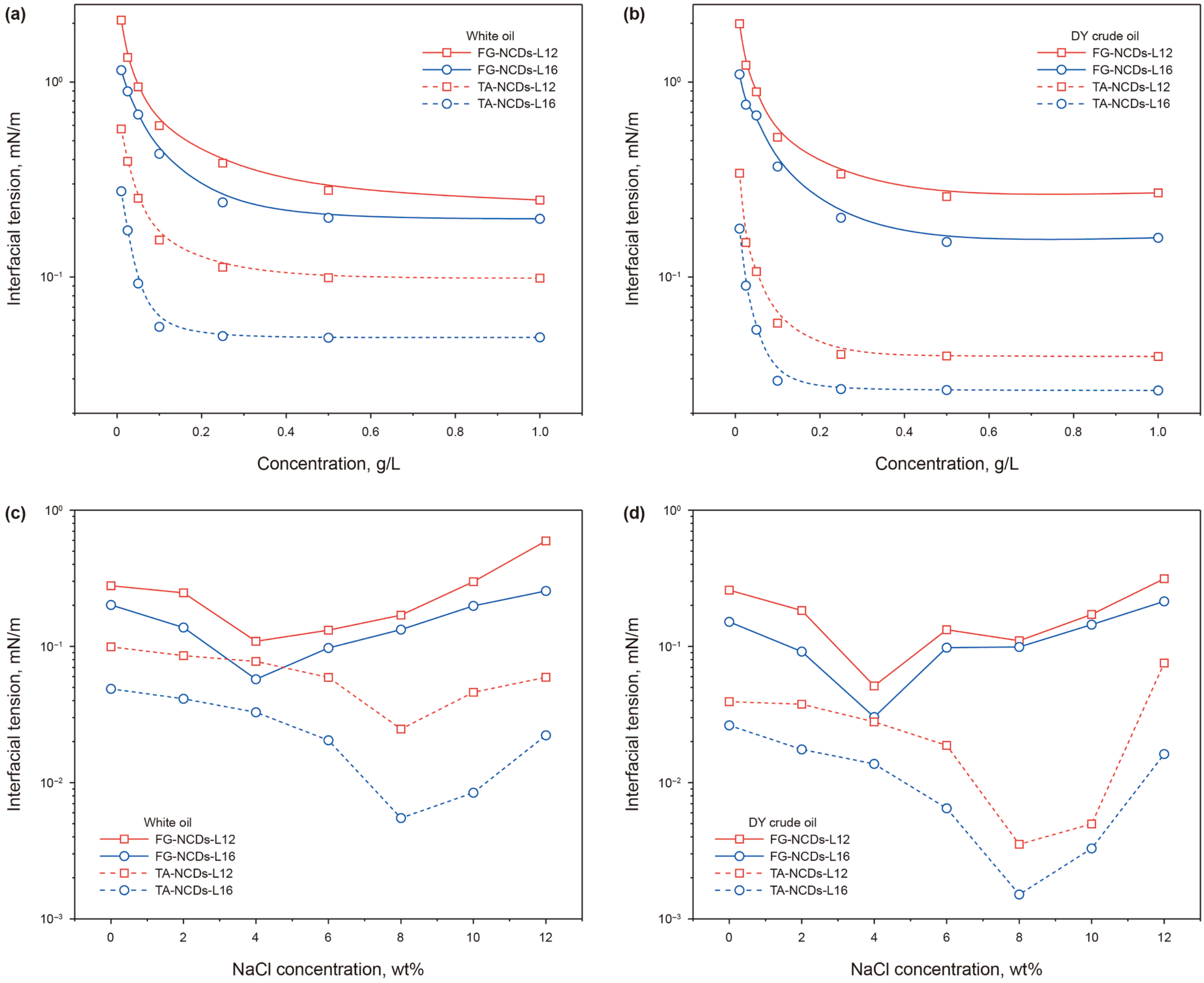

Fig. 11. Oil–water interfacial tension of amphiphilic NCDs under different concentrations and salinity conditions: (**a**, **c**) white oil as the oil phase; (**b**, **d**) DY crude oil as the oil phase.

capacity of the surfactant and the degree of alkyl chain insertion. In contrast, DY crude oil contains a substantial proportion of aromatic hydrocarbons, resins, and trace amounts of asphaltenes, which possess inherent interfacial activity. These components can synergize with amphiphilic NCDs at the oil–water interface to form composite interfacial films, resulting in further reduction of interfacial free energy under identical conditions. Fig. 11(c) and (d) further illustrate the response of interfacial tension to varying NaCl concentrations at a fixed NCD concentration of 0.5 g/L. Overall, the interfacial tension initially decreased significantly with increasing salt concentration, reaching a minimum before gradually rising again. In the white oil system, FG-NCDs-L12 and FG-NCDs-L16 achieved their lowest values of 0.10898 and 0.05737 mN/m at 4 wt% NaCl, whereas TA-NCDs-L12 and TA-NCDs-L16 reached lower interfacial tensions of 0.02472 and 0.00549 mN/m at 8 wt%. A similar but more pronounced trend was observed in the DY crude oil system, where TA-NCDs-L16 reduced the interfacial tension to as low as 0.00151 mN/m at 8 wt% NaCl, demonstrating exceptional salt resistance and interfacial activity.

This salt-resistance effect can be attributed to multiple interfacial regulation mechanisms triggered by salt ions. At low to moderate NaCl concentrations, the ionic shielding effect reduces electrostatic repulsion between polar groups in the aqueous phase, thereby promoting the formation of compact and well-ordered adsorption films of amphiphilic NCD molecules at the oil–water interface, which significantly lowers interfacial free energy (Vera et al., 2020). Simultaneously, the dehydration effect induced by salt decreases the thickness of the hydration layer, facilitating the insertion of hydrophobic chains into the oil phase and further enhancing interfacial activity. However, at higher salt concentrations, interfacial adsorption becomes less efficient due to competitive ion adsorption, disruption of the structured ion layers at the interface, and partial aggregation of carbon dot micelles. These effects result in a gradual increase in interfacial tension (Lu et al., 2024; Wu et al., 2025a). Benefiting from the synergistic effect of their higher density of quaternary ammonium groups and flexible long hydrophobic chains, TA-series NCDs are capable of maintaining a stable and continuous interfacial adsorption layer even under high salinity, exhibiting outstanding salt resistance and ultra-low interfacial tension regulation. Moreover, in the DY crude oil system, the complex composition of the oil phase may further promote the formation of synergistic interfacial assemblies with the polar functional groups on NCD surfaces under high-salinity conditions. This cooperative interaction enhances the compactness and stability of the composite interfacial film, pushing the interfacial tension to ultra-low levels. Such a synergistic adsorption mechanism is particularly critical for complex reservoir environments, as it improves oil–water displacement efficiency, reduces capillary resistance, and facilitates favorable flow redistribution. These findings provide clear molecular-level insights and theoretical guidance for interfacial regulation strategies in high-salinity oil displacement systems.

3.3. Enhanced oil recovery performance of amphiphilic NCDs

Fig. 12 presents the oil displacement performance of four amphiphilic NCD-based agents in low-permeability and low-porosity cores, highlighting a clear structure–performance correlation. The entire displacement process is divided into three stages: initial water flooding, chemical flooding, and subsequent water flooding.

In the initial water flooding stage, the injection pressure gradually increases with continued brine injection until it stabilizes, while the oil recovery gradually rises and eventually levels off. During this stage, the stabilized injection pressures corresponding to the four carbon dot systems were 7.08 MPa for FG-NCDs-L12, 6.99 MPa for FG-NCDs-L16, 6.96 MPa for TA-NCDs-L12, and 6.82 MPa for TA-NCDs-L16. The corresponding stabilized oil recovery rates were 32.19%, 32.94%, 32.76%, and 33.16%, respectively. These results indicate that in the initial water flooding stage, oil recovery remained relatively low due to the strongly oil-wet state of the core surfaces and high capillary resistance.

In the chemical flooding stage, all NCD-based agents significantly reduced the injection pressure required for oil displacement while enhancing the oil recovery. Among them, TA-NCDs-L16 exhibited the best performance, with an injection pressure as low as 1.42 MPa. This value was substantially lower than those of FG-NCDs-L12 (3.25 MPa), FG-NCDs-L16 (2.76 MPa), and TA-NCDs-L12 (2.20 MPa), resulting in a corresponding oil recovery of 49.40%. This marked reduction in injection pressure and improvement in recovery can be attributed to the synergistic effects of efficient pore-wall adsorption, wettability reversal, and ultra-low interfacial tension provided by the amphiphilic NCDs. As previously confirmed in the interfacial performance assessments, the TA-series carbon dots possess higher densities of quaternary ammonium cations and longer alkyl hydrophobic chains. These structural features enable the formation of denser and more stable polar reconstruction adsorption layers on hydrophobic surfaces, which substantially weaken the adhesion of oil to the rock matrix, disrupt the strongly oil-wet structure, reduce capillary resistance and retention pressure, and thereby facilitate the detachment and migration of residual oil (Xiang et al., 2024). This micro-scale stripping effect is particularly enhanced in the TA-NCDs-L16 system due to its higher polarity density and flexible alkyl segments. Additionally, the extremely low permeability (0.3–0.5 mD) and porosity (10%–12%) of the cores imply narrow throats and confined flow channels. Benefiting from their ultra-small size (2–5 nm), excellent interfacial activity (interfacial tension as low as 0.00151 mN/m), and strong wettability alteration capability

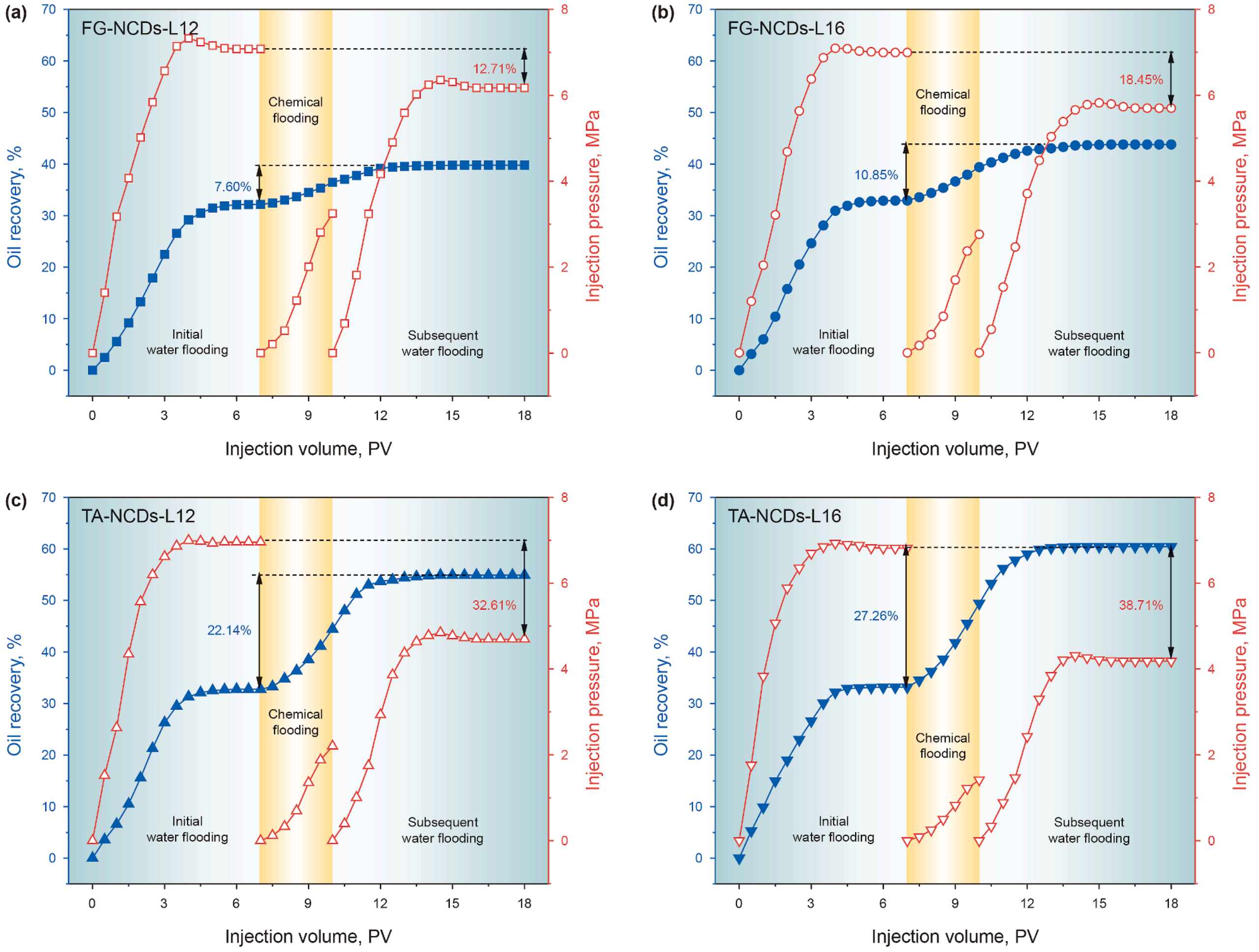

Fig. 12. Oil recovery and injection pressure of amphiphilic NCD flooding systems: (**a**) FG-NCDs-L12; (**b**) FG-NCDs-L16; (**c**) TA-NCDs-L12; (**d**) TA-NCDs-L16.

(contact angle reduced from over 90° to as low as 16.3°), the amphiphilic NCDs can achieve sufficient dispersion and stable adsorption within the narrow pore spaces. Simultaneously, they form flexible and compact interfacial layers at the oil–water interface, significantly reducing interfacial tension while enhancing the detachment and redistribution of trapped oil droplets in micropores (Cao et al., 2023b; Shen et al., 2024). These advantages collectively enable the amphiphilic NCDs to exhibit superior oil displacement performance under low-permeability reservoir conditions.

During the subsequent water flooding stage, the injection pressure was significantly reduced compared to the initial water flooding, primarily due to the substantial alteration in core wettability caused by the injection and 24 h aging of amphiphilic NCDs during the chemical flooding phase. Specifically, the stabilized pressures for FG-NCDs-L12, FG-NCDs-L16, TA-NCDs-L12, and TA-NCDs-L16 decreased by 12.71%, 18.45%, 32.61%, and 38.71%, respectively. The corresponding incremental oil recoveries were 7.60%, 10.85%, 22.14%, and 27.26%, resulting in final total recovery efficiencies of 39.79%, 43.79%, 54.90%, and 60.42%, respectively. These results reaffirm the sustained effect of the polar adsorption layers formed by the carbon dots on enhancing core wettability and mitigating capillary retention.

Overall, the TA-series NCDs exhibited superior oil displacement performance, with TA-NCDs-L16 achieving the best results. This can be attributed to multiple synergistic mechanisms, including ultra-low interfacial tension, efficient wettability reversal, reduced flow resistance, and excellent salt tolerance. These interfacial effects highlight the exceptional capacity of amphiphilic carbon dots to regulate oil–water interactions and alter surface energetics under complex reservoir conditions. The findings provide robust experimental evidence and mechanistic insight supporting the application of nanosurfactant-assisted flooding in the development of high-salinity, low-permeability reservoirs.

3.4. *Comprehensive evaluation of amphiphilic NCDs in low-permeability reservoirs*

To further validate the adaptability and application potential of amphiphilic NCDs under realistic low-permeability reservoir conditions, FG-NCDs-L16 and TA-NCDs-L16 were selected as representative samples with superior interfacial performance. At a fixed concentration of 0.5 g/L, their wettability regulation, interfacial tension reduction, and oil displacement capacity were systematically investigated in formation water with a high salinity of approximately 99.95 g/L (containing 21.56 g/L Ca^{2+} and 0.20 g/L Mg^{2+}) across a range of temperatures. In addition, their long-term stability under these conditions was assessed.

Contact angle measurements are presented in Fig. 13(a) and (b). In the formation water system, as the immersion temperature increased from 50 to 90 °C (with a fixed treatment time of 24 h), both amphiphilic NCDs exhibited enhanced wettability reversal. Specifically, the contact angle of FG-NCDs-L16 decreased from 64.51° to 56.69°, while that of TA-NCDs-L16 further decreased from 34.13° to 27.62°. Considering that the reservoir temperature of interest typically falls within the range of 60–80 °C, the aging effect at 80 °C was further examined. The results showed that wettability reversal mainly occurred during the initial stage (0–24 h). The contact angle of FG-NCDs-L16 dropped sharply from 94.72° to 57.12° and stabilized at 51.21° after 240 h, while TA-NCDs-L16 decreased from 93.61° to 28.05° and further stabilized at 23.92° after 240 h. Overall, TA-NCDs-L16 consistently exhibited lower and more stable contact angles across the entire temperature range and aging periods. These observations suggest that in a high-salinity environment, the compression of the electrical double layer and the interfacial dehydration effect induced by Ca^{2+} and Mg^{2+} facilitate the firm adsorption of carbon dot molecules on oil-wet surfaces, leading to the formation of a polar-oriented adsorption layer. At the same time, increasing temperature enhances molecular thermal motion, which drives the interfacial adsorption layer to rearrange into a more ordered and compact structure, thereby improving the persistence and stability of wettability reversal. Compared with FG-NCDs-L16, TA-NCDs-L16 benefits from a higher density of quaternary ammonium sites and hydrophobic chains, enabling it to maintain a robust adsorption layer under both ionic shielding and thermal perturbation, thus demonstrating superior wettability control performance.

Oil–water interfacial tension tests further verified the interfacial regulation capability of the amphiphilic NCDs (Fig. 13(c) and (d)). Within the temperature range of 50–90 °C, both samples exhibited good thermal adaptability and salt tolerance, as the interfacial tension between DY crude oil and the formation water systems gradually decreased with increasing temperature and then stabilized. This behavior can be attributed to the weakening of hydrogen bonding between water molecules and the hydrophilic groups on the NCD surface, as well as the intensified thermal motion of oil and water molecules at elevated temperatures, which enhances the hydrophobicity of the NCDs and promotes higher adsorption at the oil–water interface, thereby lowering the interfacial tension (Zhang et al., 2025). Owing to its higher density of long-chain hydrophobic groups, TA-NCDs-L16 consistently showed superior interfacial activity compared with FG-NCDs-L16 across all tested temperatures. During long-term aging at 80 °C, FG-NCDs-L16 exhibited a trend of initial decrease followed by a slight increase, with interfacial tension remaining at a relatively low level (rising slightly from 0.11055 to 0.11210 mN/m), indicating no obvious deactivation. In contrast, TA-NCDs-L16 maintained ultra-low interfacial tension throughout, gradually decreasing from 0.00237 to 0.00212 mN/m, which demonstrates its exceptional stability under complex saline conditions and prolonged thermal treatment. It is noteworthy that, compared with results obtained in 10 wt% NaCl solution of similar salinity (Fig. 11(d)), the interfacial tensions of FG-NCDs-L16 and TA-NCDs-L16 in formation water decreased from 0.14450 to 0.00329 mN/m to 0.12383 and 0.00263 mN/m, respectively (measured at 60 °C with zero aging time). For DY crude oil, which contains abundant saturates and aromatics, the introduction of divalent ions such as Ca^{2+} and Mg^{2+} can strengthen non-covalent interactions with hydrocarbon components. Compared with monovalent ions alone, these interactions further facilitate interfacial adsorption and are more effective in reducing interfacial tension (Kakati and Sangwai, 2017).

Core flooding experiments further revealed the displacement characteristics of amphiphilic NCDs under complex reservoir conditions (Fig. 13(e) and (f)). In low-permeability cores, the total oil recovery of the FG-NCDs-L16 system showed a slight increase with rising temperature, reaching 41.31% at 90 °C, corresponding to a 7.35% increment over the initial water flooding, accompanied by a 13.86% reduction in injection pressure. In contrast, the TA-NCDs-L16 system consistently exhibited superior performance across the tested temperature range, achieving an oil recovery increment of 26.24% and a total recovery of 60.13% at 90 °C, with injection pressure reduced by 37.73%. These results indicate that the TA-series carbon dots, owing to their higher density of quaternary ammonium groups and hydrophobic chains, retain strong interfacial activity in the presence of Ca^{2+} and Mg^{2+}. This enables them to sustain stable interfacial adsorption layers and efficient wettability reversal, thereby maintaining excellent displacement performance under high salinity and elevated temperature conditions (Yao et al., 2021, 2022).

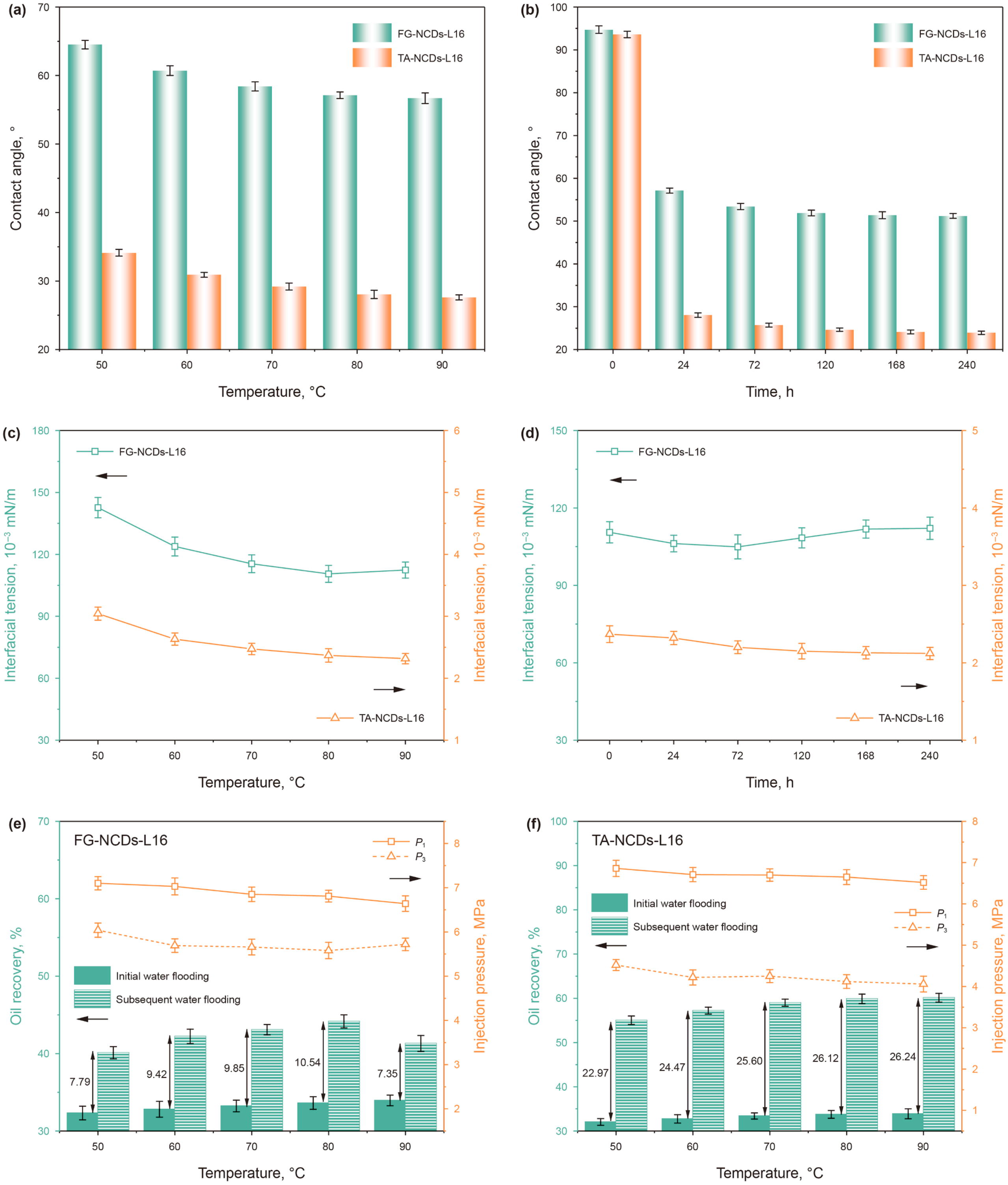

Fig. 13. Comprehensive evaluation of FG-NCDs-L16 and TA-NCDs-L16 in formation water: contact angle variation with temperature (**a**) and aging time (**b**); oil–water interfacial tension with temperature (**c**) and aging time (**d**); oil recovery and injection pressure in core flooding at different temperatures for FG-NCDs-L16 (**e**) and TA-NCDs-L16 (**f**).

Overall, the results demonstrate that amphiphilic NCDs can effectively induce wettability reversal and maintain significant reductions in oil–water interfacial tension in high-salinity formation water enriched with Ca^{2+} and Mg^{2+}. With increasing temperature, the interfacial adsorption layer becomes more compact, resulting in lower injection pressures and higher oil recovery efficiencies. In comparison, TA-NCDs-L16 consistently sustains ultra-low interfacial tension and long-lasting wettability reversal across the studied temperature range and during prolonged thermal aging, leading to more substantial recovery increments during subsequent water flooding. These findings align with the structural performance framework established through the synergy of high-density quaternary ammonium groups and long hydrophobic chains, highlighting the strong adaptability and engineering potential of amphiphilic NCDs, particularly TA-NCDs-L16, for application in high-salinity, low-permeability reservoirs with complex ionic environments.

In addition to interfacial performance, a brief cost–benefit analysis highlights the practical feasibility of the selected precursors. Petroleum-derived precursors such as petroleum coke (418.64–837.29 USD/ton) and petroleum asphalt (488.42–558.19 USD/ton) appear less expensive at first glance, but the preparation of CDs from these feedstocks usually requires electrochemical exfoliation or strong acid oxidation (Alshoaibi and Rasheed, 2025), which involves complex processes, harsh environments, and significant purification costs, limiting their industrial scalability. In contrast, tartaric acid (1395.48–1883.90 USD/ton) is a small-molecule precursor with higher purity and simpler conversion routes, producing fewer by-products and enabling reproducible product quality. It is also noteworthy that tartaric acid can be produced from winery by-products such as grape pomace and lees through tartrate extraction and purification, further improving its economic and environmental sustainability (Yalcin et al., 2008). Importantly, tartaric acid is substantially cheaper than polysaccharide-based fenugreek gum (3488.70–6977.39 USD/ton), while still providing abundant carboxyl groups that facilitate efficient amidation and quaternization during surface functionalization. This cost–performance balance makes tartaric acid a practical and scalable precursor choice for the synthesis of amphiphilic NCDs.

4. Conclusions

In this study, a series of amphiphilic NCDs with quaternary ammonium cations as the primary hydrophilic groups were successfully synthesized using fenugreek gum and tartaric acid as biomass-derived precursors. A synergistic surface modification strategy involving amidation, quaternization, and alkylation was employed. The relationships between precursor structure, surface/interface properties, and oil displacement behavior in low-permeability reservoirs were systematically investigated. The main conclusions are summarized as follows:

(1) All synthesized carbon dots exhibited well-dispersed spherical morphology with average diameters below 5 nm. FTIR and XPS analyses confirmed the presence of quaternary ammonium salts, C–O/C–N, and C=O functional groups on the surface. The abundant carboxyl groups provided by the tartaric acid precursor significantly promoted amidation and quaternization reactions, resulting in higher surface polarity and amphiphilicity for the TA-series carbon dots. UV–Vis and PL spectroscopy further revealed that increasing the alkyl chain length enhanced the thickness of the hydrophobic surface layer, which suppressed local surface defects, leading to decreased fluorescence intensity accompanied by a slight red shift.

(2) The amphiphilic NCDs exhibited excellent interfacial activity and wettability regulation capabilities, with their performance strongly dependent on precursor structure and alkyl chain length. Among all samples, the TA-NCDs-L16 system demonstrated the best overall performance, with a CMC of 0.104 g/L and a surface tension at CMC of 24.71 mN/m. Its hydrodynamic diameter near the CMC was 197.14 nm, and the zeta potential at neutral pH reached +67.80 mV. The oil–water interfacial tension was reduced to as low as 0.026 mN/m under salt-free conditions and further decreased to 0.00151 mN/m in the presence of 8 wt% NaCl. Even at a high salt concentration of 10 wt%, an ultra-low interfacial tension of 0.00329 mN/m was maintained, indicating outstanding salt tolerance and interfacial stability. Additionally, this sample exhibited superior wettability reversal capability, achieving a minimum water contact angle of 16.3°.

(3) In low-permeability core flooding experiments, all four amphiphilic NCD systems significantly enhanced crude oil recovery. Notably, the TA-NCDs-L16 system achieved the highest recovery of 60.42%, corresponding to a 27.26% increase, while simultaneously reducing injection pressure by 38.71%. This improved recovery performance is attributed to multiple synergistic mechanisms: the ultra-low interfacial tension greatly weakens capillary confinement, the formation of a high-density polar adsorption layer effectively reduces oil–rock adhesion, and the nanoscale particle size enables superior pore throat penetration and regulation of fluid distribution within the porous media.

(4) Additional evaluations under reservoir-representative conditions confirmed that amphiphilic NCDs maintain effective wettability reversal and interfacial activity in highly mineralized formation water containing abundant Ca^{2+} and Mg^{2+} ions. The FG-NCDs-L16 exhibited stable but slightly weakened performance, while TA-NCDs-L16 consistently sustained ultra-low interfacial tension (~0.002 mN/m) and strong wettability reversal even after long-term thermal aging at 80 °C. These results demonstrate that TA-NCDs-L16, in particular, possesses excellent stability and adaptability in complex ion environments and elevated temperature conditions, highlighting its potential as a robust nanofluid EOR agent for low-permeability reservoirs.

In conclusion, this study developed biomass-derived amphiphilic NCDs with tunable interfacial activity, wettability regulation, and enhanced oil recovery performance under low-permeability conditions by tailoring precursor molecular structures and hydrophobic alkyl chain flexibility. The findings provide valuable insights and experimental reference for the design of nano-fluid-based EOR agents and the efficient development of low-permeability reservoirs.

CRediT authorship contribution statement

Yu Wu: Writing – review & editing, Writing – original draft, Visualization, Validation, Investigation, Formal analysis, Data curation. **Yan-Cheng Zheng:** Writing – review & editing, Validation, Resources, Project administration, Methodology, Funding acquisition, Conceptualization. **Jian Mu:** Investigation, Formal analysis, Data curation. **Fu-Chang You:** Writing – review & editing, Methodology, Investigation. **Zheng-Yu Li:** Investigation, Formal analysis.

Data availability

Data will be made available on request.

Declaration of competing interest

The authors declare that they have no known competing financial interests or personal relationships that could have appeared to influence the work reported in this paper.

Acknowledgements

The authors appreciate financial support from the National Natural Science Foundation of China (No. 52374030).

Supplementary data

Supplementary data to this article can be found online at https://doi.org/10.1016/j.petsci.2025.12.011.

References

Abbood, N.K., Obeidavi, A., Hosseini, S., 2022. Investigation on the effect of CuO nanoparticles on the IFT and wettability alteration at the presence of [C_{12}mim][Cl] during enhanced oil recovery processes. J. Pet. Explor. Prod. Technol. 12 (7), 1855–1866. https://doi.org/10.1007/s13202-021-01441-6.

AfzaliTabar, M., Rashidi, A., Alaei, M., Koolivand, H., Pourhashem, S., Askari, S., 2020. Hybrid of quantum dots for interfacial tension reduction and reservoir alteration wettability for enhanced oil recovery (EOR). J. Mol. Liq. 307, 112984. https://doi.org/10.1016/j.molliq.2020.112984.

Alshoaibi, A., Rasheed, T., 2025. Transforming petroleum coke into greener and sustainable carbon nanomaterials: Synthesis, structure and applications. J. Environ. Manag. 393, 127002. https://doi.org/10.1016/j.jenvman.2025.127002.

Bao, L.-N., Yang, Y.-R., Li, J.-B., Li, X., Dong, J.-X., 2024. Synthesis and structure-property relationship of coal-based isomeric alkylbenzene sulfonate surfactants. Colloids Surf. A Physicochem. Eng. Asp. 696, 134350. https://doi.org/10.1016/j.colsurfa.2024.134350.

Cai, M.-X., Lai, L., Zhao, M.-W., 2025. Synthesis, properties, and applications of amphiphilic carbon dots: A review. Carbon 233, 119921. https://doi.org/10.1016/j.carbon.2024.119921.

Cao, M.-J., Li, Y., Song, X.-G., Chen, Y.-S., Sun, L.-H., Shi, X., Dai, C.-L., Yuan, B., 2023a. Carbon dots nanofluid: Reducing injection pressure in unconventional reservoir by regulating oil/water/rock interfacial properties. Fuel 352, 129046. https://doi.org/10.1016/j.fuel.2023.129046.

Cao, X.-M., Li, Q., Myers, M., Xu, L., Chen, Q., Tan, Y.-S., 2023b. Nanofluid impact on fluid interaction and migration characteristics for enhanced oil recovery in Baikouquan tight glutenite. Adv. Geo-Energy Res. 9 (2), 94–105. https://doi.org/10.46690/ager.2023.08.03.

Delgado-Mellado, N., Larriba, M., Navarro, P., Rigual, V., Ayuso, M., Garcia, J., Rodriguez, F., 2018. Thermal stability of choline chloride deep eutectic solvents by TGA/FTIR-ATR analysis. J. Mol. Liq. 260, 37–43. https://doi.org/10.1016/j.molliq.2018.03.076.

Dibaji, A.S., Rashidi, A., Baniyaghoob, S., Shahrabadi, A., 2022. Synthesizing CNT/MgO nanocomposite to form stable pickering emulsion at high temperature and salinity and its application to improved oil displacement efficiency. Chem. Eng. Res. Des. 186, 599–609. https://doi.org/10.1016/j.cherd.2022.08.034.

Ding, H., Wei, J.-S., Xiong, H.-M., 2014. Nitrogen and sulfur co-doped carbon dots with strong blue luminescence. Nanoscale 6 (22), 13817–13823. https://doi.org/10.1039/c4nr04267k.

Ding, M.-M., Li, J.-H., Fu, X.-T., Zhou, J., Tan, H., Gu, Q., Fu, Q., 2009. Synthesis, degradation, and cytotoxicity of multiblock poly(ε-caprolactone urethane)s containing gemini quaternary ammonium cationic groups. Biomacromolecules 10 (10), 2857–2865. https://doi.org/10.1021/bm9006826.

Fan, J.-J., Cui, J.-P., He, T.-L., Zhang, T.-H., Yuan, X.-Y., Hu, J.-W., Gao, H.-T., Zhang, H., Li, C.-L., Hu, S.-Q., Sun, S.-Q., 2025. Dynamic covalent carbon dot-based emulsifiers: A novel strategy for smart Pickering emulsions and enhanced heavy oil recovery in ultra-low permeability reservoirs. J. Colloid Interface Sci. 697, 137935. https://doi.org/10.1016/j.jcis.2025.137935.

Feng, S.-Y., Jiang, Z.-W., Tang, S.-F., Hu, R.-Z., Jin, L.-J., Wang, S.-Y., Wang, R., 2022. Synthesis, interfacial activity and rheological properties of low interfacial tension viscoelastic Gemini surfactants. J. Petrol. Sci. Eng. 209, 109845. https://doi.org/10.1016/j.petrol.2021.109845.

Gao, Q.-Q., Wei, P., Lv, B.-L., Zhu, M., Qi, Y., Sun, H., 2025. Design of amphiphilic carbon dots for producing stable CO_2 foams as eco-friendly fluids for enhanced oil recovery. ACS Sustain. Chem. Eng. 13 (4), 1824–1837. https://doi.org/10.1021/acssuschemeng.4c10223.

Hu, W.-R., Wei, Y., Bao, J.-W., 2018. Development of the theory and technology for low permeability reservoirs in China. Petrol. Explor. Dev. 45 (4), 685–697. https://doi.org/10.1016/s1876-3804(18)30072-7.

Joshi, D., Kumar, A., Maurya, N.K., Mandal, A., 2025. Synthesis and characterization of carbon dots for enhanced oil recovery applications. J. Mol. Liq. 427, 127445. https://doi.org/10.1016/j.molliq.2025.127445.

Kakati, A., Sangwai, J.S., 2017. Effect of monovalent and divalent salts on the interfacial tension of pure hydrocarbon-brine systems relevant for low salinity water flooding. J. Petrol. Sci. Eng. 157, 1106–1114. https://doi.org/10.1016/j.petrol.2017.08.017.

Keykhosravi, A., Simjoo, M., 2020. Enhancement of capillary imbibition by Gamma-Alumina nanoparticles in carbonate rocks: Underlying mechanisms and scaling analysis. J. Petrol. Sci. Eng. 187, 106802. https://doi.org/10.1016/j.petrol.2019.106802.

Lashari, N., Ganat, T., Elraies, K.A., Ayoub, M.A., Kalam, S., Chandio, T.A., Qureshi, S., Sharma, T., 2022. Impact of nanoparticles stability on rheology, interfacial tension, and wettability in chemical enhanced oil recovery: A critical parametric review. J. Petrol. Sci. Eng. 212, 110199. https://doi.org/10.1016/j.petrol.2022.110199.

Li, F.-T., Wang, Z.-K., Zhou, Y., Li, L.-Z., Liu, Y.-Q., Wang, L., Li, C.-L., Zhu, H.-F., Sun, S.-Q., Hu, S.-Q., 2023a. Improvement of carbon dots corrosion inhibition by ionic liquid modification: Experimental and computational investigations. Corros. Sci. 224, 111541. https://doi.org/10.1016/j.corsci.2023.111541.

Li, L., Sun, Y., Wang, Z.-Z., Liu, J.-M., Liu, K.-Y.-W., Dai, C.-L., Wu, Y.-N., 2023b. Two-step hydrothermal synthesis of active carbon-dots with high temperature and salt resistance for injection pressure reduction and enhanced oil recovery. Colloids Surf. A Physicochem. Eng. Asp. 676, 132115. https://doi.org/10.1016/j.colsurfa.2023.132115.

Li, Y.-Y., Dai, C.-L., Zhou, H.-D., Wang, X.-K., Lv, W.-J., Zhao, M.-W., 2018a. Investigation of spontaneous imbibition by using a surfactant-free active silica water-based nanofluid for enhanced oil recovery. Energy Fuels 32 (1), 287–293. https://doi.org/10.1021/acs.energyfuels.7b03132.

Li, Y.-F., Wang, M.-X., Sun, D.-J., Li, Y.-J., Wu, T., 2018b. Effective removal of emulsified oil from oily wastewater using surfactant-modified sepiolite. Appl. Clay Sci. 157, 227–236. https://doi.org/10.1016/j.clay.2018.02.014.

Li, Y., Lai, L., Mei, P., Zhang, W.-X., Li, Y.-H., Cheng, L., Wang, Y.-Q., Liu, Y., 2019. Surface properties and solubility enhancement of Gemini/conventional surfactant mixtures based on sulfonate Gemini surfactant. J. Mol. Liq. 276, 488–496. https://doi.org/10.1016/j.molliq.2018.12.038.

Liu, J.-M., Sun, Y., Wang, X.-L., Li, L., Dai, C.-L., 2024. Carbon dot nanomaterials with high interfacial activity for unconventional reservoir development. ACS Appl. Nano Mater. 7 (8), 9305–9313. https://doi.org/10.1021/acsanm.4c00822.

Liu, Y.-L., Li, M., Lu, X.-B., Yu, J.-Z., Zhang, Z.-Z., She, Y.-H., Zhang, F., 2025. Synthesis of water-soluble and stable carbon quantum dot nanofluid mediated by *Scenedesmus* extract for enhanced crude oil recovery. Phys. Fluids 37 (2), 022037. https://doi.org/10.1063/5.0254566.

Lu, R.-L., He, S.-Y., Wang, T.-F., Lai, L., Zhao, M.-W., 2024. Low-cost preparation of temperature-resistant and salt-tolerant amphiphilic carbon dots from a nonionic surfactant and its application in enhanced oil recovery. Carbon 225, 119104. https://doi.org/10.1016/j.carbon.2024.119104.

Lu, X.-B., Zheng, Y.-C., Zhang, G.-Q., You, F.-C., 2025. Novel polyethylene glycol-based cationic Gemini surfactants for enhancing oil displacement efficiency of silica nanoparticles fluids. J. Ind. Eng. Chem. 151, 692–699. https://doi.org/10.1016/j.jiec.2025.04.040.

Medina, O.E., Rosales, S., Garzon, N., Lopez, D., Taborda, E.A., Ordonez, J.C., Fernandez, S.A., Cortes, F.B., Franco, C.A., 2024. Advances in quantum dot applications for the oil and gas industry: Current trends and future directions. Energy Fuels 38 (22), 21793–21831. https://doi.org/10.1021/acs.energyfuels.4c03984.

Meng, L.-M., Dai, Y.-J., Zhao, M.-W., Zhang, Z.-L., Dai, C.-L., Wu, Y.-N., 2024. Investigation of carbon-based nanofluid imbibition processes in low-permeability reservoirs using nuclear magnetic resonance. Colloids Surf. A Physicochem. Eng. Asp. 695, 134310. https://doi.org/10.1016/j.colsurfa.2024.134310.

Ngouangna, E.N., Jaafar, M.Z., Norddin, M.N.A.M., Agi, A., Oseh, J.O., Mamah, S., 2022. Surface modification of nanoparticles to improve oil recovery mechanisms: A critical review of the methods, influencing parameters, advances and prospects. J. Mol. Liq. 360, 119502. https://doi.org/10.1016/j.molliq.2022.119502.

Nourafkan, E., Gardy, J., Asachi, M., Ahmed, W., Wen, D.-S., 2019. Nanoparticle formation in stable microemulsions for enhanced oil recovery application. Ind. Eng. Chem. Res. 58 (28), 12664–12677. https://doi.org/10.1021/acs.iecr.9b00760.

Pan, L., Li, G.-X., Wang, Z.-Y., Liu, D.-B., Zhu, W.-K., Tong, C.-Y., Zhu, R.-L., Hu, S., 2021. Carbon dots as environment-friendly and efficient corrosion inhibitors for Q235 steel in 1 M HCl. Langmuir 37 (49), 14336–14344. https://doi.org/10.1021/acs.langmuir.1c02182.

Razavifar, M., Khoshsima, A., Riazi, M., Sheng, J.J., Esmaeilnezhad, E., 2024. Recent developments, challenges, and prospects of carbon dots (CDs) for fluid flow investigation in porous media. Petrol. Res. 9 (4), 553–564. https://doi.org/10.1016/j.ptlrs.2024.04.004.

Ren, S.-M., Cui, M.-J., Chen, X.-Y., Mei, S.-X., Qiang, Y.-J., 2022. Comparative study on corrosion inhibition of N doped and N,S codoped carbon dots for carbon steel in strong acidic solution. J. Colloid Interface Sci. 628, 384–397. https://doi.org/10.1016/j.jcis.2022.08.070.

Rezvani, H., Khalilnezhad, A., Ganji, P., Kazemzadeh, Y., 2018. How ZrO_2 nanoparticles improve the oil recovery by affecting the interfacial phenomena in the reservoir conditions? J. Mol. Liq. 252, 158–168. https://doi.org/10.1016/j.molliq.2017.12.138.

Shahan, S.M., Aiad, I., E-Sukkary, M.M., Soliman, E.A., El-Awady, M.Y., 2017. Synthesis of newly cationic surfactant based on dimethylaminopropyl amine and their silver nanoparticles: Characterization; surface activity and biological activity. Chin. Chem. Lett. 28 (2), 264–273. https://doi.org/10.1016/j.cclet.2016.09.010.

Sharma, N.K., Singh, M., Bhattarai, A., 2016. Hydrophobic study of increasing alkyl chain length of platinum surfactant complexes: Synthesis, characterization, micellization, thermodynamics, thermogravimetrics and surface morphology. RSC Adv. 6 (93), 90607–90623. https://doi.org/10.1039/c6ra20330b.

Shen, M., Zhang, C.-J., Yan, X., Wang, L., Wu, Y.-N., Jin, X., 2024. Research progress and prospects of utilizing carbon-based nanomaterials in enhanced oil recovery. Adv. Geo-Energy Res. 14 (3), 201–214. https://doi.org/10.46690/ager.2024.12.05.

Sun, Y., Dong, Y.-B., Zhu, Z.-X., Li, L., Dai, C.-L., Wu, Y.-N., Zhao, M.-W., 2023. Carbon-based active nanoparticles with ultrahigh temperature and salt resistance for enhanced oil recovery from unconventional oil reservoirs. Energy Fuels 37 (19), 14882–14890. https://doi.org/10.1021/acs.energyfuels.3c02679.

Suting, S., Wagay, T.A., Charingia, A., Askari, H., 2023. Binary micellar schemes of cationic gemini and conventional surfactants: Chain length effect. J. Dispersion Sci. Technol. 44 (11), 2001–2012. https://doi.org/10.1080/01932691.2022.2056479.

Tan, L.J., Wang, H.D., Wang, J.T., 2011. Preparation and characterization of two new kinds of soluble quaternary ammonium salts of chitosan. Advanced Materials Research, pp. 496–500. https://doi.org/10.4028/www.scientific.net/AMR.239-242.496.

Toma, S.H., Santos, J.J., da Silva, D.G., Toma, H.E., Araki, K., Huila, M.F.G., 2022. Improving stability of iron oxide nanofluids for enhanced oil recovery: Exploiting wettability modifications in carbonaceous rocks. J. Petrol. Sci. Eng. 212, 110311. https://doi.org/10.1016/j.petrol.2022.110311.

Vera, R.E., Salazar-Rodriguez, F., Marquez, R., Forgiarini, A.M., 2020. How the influence of different salts on interfacial properties of surfactant-oil-water systems at optimum formulation matches the hofmeister series ranking. J. Surfactants Deterg. 23 (3), 603–615. https://doi.org/10.1002/jsde.12406.

Wang, Y.-P., Wang, Q.-X., Han, Y.-G., Zheng, C.-L., Jiang, C.-Y., Wang, C.-Y., Zhang, L.-L., 2023. The structure effect on the physicochemical properties of Gemini surfactants used as viscosity reducer for heavy oil. J. Mol. Liq. 390, 123055. https://doi.org/10.1016/j.molliq.2023.123055.

Wu, Y.-N., Li, Y., Cao, M.-J., Dai, C.-L., He, L., Yang, Y.-P., 2020. Preparation and stabilization mechanism of carbon dots nanofluids for drag reduction. Pet. Sci. 17 (6), 1717–1725. https://doi.org/10.1007/s12182-020-00503-4.

Wu, Y.-N., Cao, M.-J., Zhao, Q.-S., Wu, X.-C., Guo, F., Tang, L.-S., Tan, X.-J., Wu, W.-T., Shi, Y.-F., Dai, C.-L., 2021. Novel high-hydrophilic carbon dots from petroleum coke for boosting injection pressure reduction and enhancing oil recovery. Carbon 184, 186–194. https://doi.org/10.1016/j.carbon.2021.08.018.

Wu, Y.-N., Tang, L.-S., Liu, D.-Y., Kong, D.-M., Kai, L., Cao, M.-J., Zhao, Q.-S., 2023. *In-situ* synthesis of high thermal stability and salt resistance carbon dots for injection pressure reduction and enhanced oil recovery. Nano Res. 16 (10), 12058–12065. https://doi.org/10.1007/s12274-022-5083-y.

Wu, Y., Song, H.-L., Zheng, Y.-C., You, F.-C., Chang, S.-T., Zhu, S.-H., 2025a. Amphiphilic nitrogen-doped carbon dots derived from bituminous coal: Enhanced oil-water interfacial activity and nanomaterial dispersibility. Fuel Process. Technol. 275, 108261. https://doi.org/10.1016/j.fuproc.2025.108261.

Wu, Y., Zeng, L.-C., Zheng, Y.-C., You, F.-C., Liu, X.-J., 2025b. Pectin-derived nitrogen-doped carbon dots as green corrosion inhibitors for N80 steel in 1 M sulfuric acid solution. Appl. Surf. Sci. 687, 162245. https://doi.org/10.1016/j.apsusc.2024.162245.

Wyss, H.M., Blair, D.L., Morris, J.F., Stone, H.A., Weitz, D.A., 2006. Mechanism for clogging of microchannels. Phys. Rev. E 74, 061402. https://doi.org/10.1103/PhysRevE.74.061402.

Xiang, W., Sun, Y., Li, L., Wang, X.-L., Zhao, M.-W., Dai, C.-L., 2024. Long carbon chain-modified carbon nanoparticles for oil displacement in harsh-condition reservoirs. J. Mol. Liq. 406, 125039. https://doi.org/10.1016/j.molliq.2024.125039.

Xu, Z.-X., Gan, Y., Zeng, J., Chen, J.-D., Fu, A.-Q., Zheng, X.-W., Li, W.-P., 2023. Green synthesis of functionalized fluorescent carbon dots from biomass and their corrosion inhibition mechanism for copper in sulfuric acid environment. Chem. Eng. J. 470, 144425. https://doi.org/10.1016/j.cej.2023.144425.

Yalcin, D., Ozcalik, O., Altiok, E., Bayraktar, O., 2008. Characterization and recovery of tartaric acid from wastes of wine and grape juice industries. J. Therm. Anal. Calorim. 94 (3), 767–771. https://doi.org/10.1007/s10973-008-9345-z.

Yang, J., Yang, Y.-H., Su, L.-J., Tao, X., Zhang, J.-T., Chen, Y., Yang, L.-J., 2023. Diethylenetriamine-ll-CD-modified carbon quantum dots for selective fluorescence sensing of Hg^{2+} and Fe^{3+} and cellular imaging. Spectrochim. Acta Mol. Biomol. Spectrosc. 291, 122364. https://doi.org/10.1016/j.saa.2023.122364.

Yao, Y., Wei, M.-Z., Bai, B.-J., 2022. Descriptive statistical analysis of experimental data for wettability alteration with surfactants in carbonate reservoirs. Fuel 310, 122110. https://doi.org/10.1016/j.fuel.2021.122110.

Yao, Y., Wei, M.-Z., Kang, W.-L., 2021. A review of wettability alteration using surfactants in carbonate reservoirs. Adv. Colloid Interface Sci. 294, 102477. https://doi.org/10.1016/j.cis.2021.102477.

Ye, Y.-W., Zhang, D.-W., Zou, Y.-J., Zhao, H.-C., Chen, H., 2020. A feasible method to improve the protection ability of metal by functionalized carbon dots as environment-friendly corrosion inhibitor. J. Clean. Prod. 264, 121682. https://doi.org/10.1016/j.jclepro.2020.121682.

Yekeen, N., Salampessy, S.N., Abu Bakar, A.H., Ali, M., Okunade, O.A., Musa, S.A., Bavoh, C.B., 2023. Synthesis and pore-scale visualization studies of enhanced oil recovery mechanisms of rice straw silica nanoparticles. Geoenergy Sci. Eng. 221, 111292. https://doi.org/10.1016/j.petrol.2022.111292.

Zargar, G., Arabpour, T., Manshad, A.K., Ali, J.A., Sajadi, S.M., Keshavarz, A., Mohammadi, A.H., 2020. Experimental investigation of the effect of green TiO_2/Quartz nanocomposite on interfacial tension reduction, wettability alteration, and oil recovery improvement. Fuel 263, 116599. https://doi.org/10.1016/j.fuel.2019.116599.

Zhang, B.-P., Zhang, H., Wang, Y., Fang, S.-Y., 2022. Adsorption behavior and mechanism of amine/quaternary ammonium lignin on tungsten. Int. J. Biol. Macromol. 216, 882–890. https://doi.org/10.1016/j.ijbiomac.2022.07.226.

Zhang, J., Zhao, C.-H., Wang, X.-J., Liu, Y.-G., Xiong, S.-Q., Liu, C.-L., Yang, Y., 2025. Preparation of amphiphilic carbon dots with high interfacial activity for depressurization and enhanced oil recovery in low permeability reservoirs. J. Mol. Liq. 433, 127945. https://doi.org/10.1016/j.molliq.2025.127945.

Zhao, M.-W., Liu, K.-W., Meng, X.-J., Ma, Z.-F., Dai, C.-L., 2024. Review on principles, influence and applications of nanomaterials in enhancing oil recovery. Fuel 371, 131985. https://doi.org/10.1016/j.fuel.2024.131985.

Zhao, M.-W., Lv, W.-J., Li, Y.-Y., Dai, C.-L., Wang, X.-K., Zhou, H.-D., Zou, C.-W., Gao, M.-W., Zhang, Y., Wu, Y.-N., 2018. Study on the synergy between silica nanoparticles and surfactants for enhanced oil recovery during spontaneous imbibition. J. Mol. Liq. 261, 373–378. https://doi.org/10.1016/j.molliq.2018.04.034.

Zhao, M.-W., Song, X.-G., Zhou, D., Lv, W.-J., Dai, C.-L., Yang, Q.-R., Li, Y., Zhang, B.-H., Zhao, Y.-R., Wu, Y.-N., 2020. Study on the reducing injection pressure regulation of hydrophobic carbon nanoparticles. Langmuir 36 (15), 3989–3996. https://doi.org/10.1021/acs.langmuir.0c00115.

Zhou, Y.-X., Shan, Y.-F., Xiao, L.-H., Song, X., Bao, W.-B., Ma, H., Li, H., Wu, X.-Y., Wang, R.-R., 2025. Modified carbon quantum dots based nanocomposite system for enhanced oil recovery in low permeability reservoir. Energy Fuels 39 (9), 4204–4220. https://doi.org/10.1021/acs.energyfuels.4c05872.

Zhou, Y.-X., Wu, X., Zhong, X., Zhang, S.-J., Pu, H., Zhao, J.X.-J., 2020. Development of silicon quantum dots based nano-fluid for enhanced oil recovery in tight Bakken cores. Fuel 277, 118203. https://doi.org/10.1016/j.fuel.2020.118203.

Zhu, M.-Y., He, Z.-Y., Guo, L., Zhang, R.-H., Anadebe, V.C., Obot, I.B., Zheng, X.-W., 2021. Corrosion inhibition of eco-friendly nitrogen-doped carbon dots for carbon steel in acidic media: Performance and mechanism investigation. J. Mol. Liq. 342, 117583. https://doi.org/10.1016/j.molliq.2021.117583.